# Stability and receptivity characteristics of a laminar separation bubble on an aerofoil

L. E. JONES†, R. D. SANDBERG
AND N. D. SANDHAM

Aerodynamics and Flight Mechanics Research Group, School of Engineering Sciences,
University of Southampton, Southampton SO17 1BJ, UK

Stability characteristics of aerofoil flows are investigated by linear stability analysis of time-averaged velocity profiles and by direct numerical simulations with time-dependent forcing terms. First the wake behind an aerofoil is investigated, illustrating the feasibility of detecting absolute instability using these methods. The time-averaged flow around an NACA-0012 aerofoil at incidence is then investigated in terms of its response to very low-amplitude hydrodynamic and acoustic perturbations. Flow fields obtained from both two- and three-dimensional simulations are investigated, for which the aerofoil flow exhibits a laminar separation bubble. Convective stability characteristics are documented, and the separation bubble is found to exhibit no absolute instability in the classical sense; i.e. no growing disturbances with zero group velocity are observed. The flow is however found to be globally unstable via an acoustic-feedback loop involving the aerofoil trailing edge as a source of acoustic excitation and the aerofoil leading-edge region as a site of receptivity. Evidence suggests that the feedback loop may play an important role in frequency selection of the vortex shedding that occurs in two dimensions. Further simulations are presented to investigate the receptivity process by which acoustic waves generate hydrodynamic instabilities within the aerofoil boundary layer. The dependency of the receptivity process to both frequency and source location is quantified. It is found that the amplitude of trailing-edge noise in the fully developed simulation is sufficient to promote transition via leading-edge receptivity.

## 1. Introduction

Over the past decade the study of low-Reynolds-number aerodynamics has increased in importance because of the development of small unmanned air vehicles (UAVs) and micro air vehicles (MAVs), which operate at much lower Reynolds numbers than manned aircraft. For example, in the case of MAVs aerofoil chord lengths will typically be of the order of centimetres, and flight Reynolds numbers may be as low as 42 000 (Torres & Mueller 2001). In contrast to high-Reynolds-number flows which are mostly turbulent, at low Reynolds numbers boundary layers are expected to remain laminar for a significant percentage of the aerofoil chord. Laminar boundary layers are prone to separate under the influence of an adverse pressure gradient and upon separating become highly unstable; hence the

† Email address for correspondence: ljones@soton.ac.uk

onset of transition is usually rapid. Conversely, transition to turbulence within an attached boundary layer can delay the onset of separation, and hence the process of separation is coupled strongly with that of transition to turbulence. The aerodynamic performance of lifting bodies at low Reynolds numbers is therefore highly dependent upon the transition process, and a modest change in aerofoil incidence, background turbulence level or fluid velocity may cause a significant change in the location of transition and/or separation and for certain cases may result in stall. Understanding the physics of the transition process is clearly vital to accurately predict low-Reynolds-number flows and has historically been one of the most active research topics within the field of fluid dynamics. The current study considers transition of wall-bounded shear flows, which has been the subject of many reviews, one of the more recent being Kachanov (1994). A brief summary is provided here, based upon Morkovin's road map for transition (Morkovin, Reshotko & Herbert 1994).

For the case of aerofoil flow, transition is initiated either by surface roughness/vibration or by external stimuli such as vortical perturbations or sound waves impinging on the aerofoil boundary layer. A receptivity process then ensues, whereby the perturbations generate instability waves within the boundary layer. Ignoring here bypass transition (Morkovin 1984), where disturbances are so large that transition occurs immediately with no discernible intermediate stages, the next stage in the process is growth of the instability waves in an exponential fashion, termed primary instability. When perturbations have reached nonlinear amplitudes ($\sim O(1 \times 10^{-2})$) secondary instabilities occur, e.g the formation of $\Lambda$ vortices, upon the primary instability structure, before higher instabilities and finally the breakdown to small scales and turbulent flow. For a review of coherent structures associated with higher instabilities, see Sandham & Kleiser (1992) and Lee & Wu (2008).

Since the process of primary instability growth takes place over longer time scales than the subsequent breakdown to turbulence that occurs upon reaching nonlinear amplitudes, approximate transition predictions can be performed by considering only this stage. Primary instability growth may be predicted by employing linear stability theory (LST), where the governing equations are linearized, neglecting viscous terms, and disturbances are assumed to take the form of normal-mode perturbations periodic in time and typically periodic in one or more spatial directions (Schmid, Henningson & Jankowski 2002). Following this procedure for the case of incompressible parallel flow yields the well-known Orr–Sommerfeld equation, the eigensolutions of which describe primary instability waves. Increasing in complexity, the parabolized stability equations account for modest streamwise variations in the base flow (Herbert 1997), whilst performing two- and three-dimensional linear stability analyses, procedures that have been termed 'BiGlobal' and 'TriGlobal' analyses, allows investigation of complex geometries (Theofilis 2003). At this stage it is helpful to distinguish between absolute and convective instabilities (Gaster 1963, 1968), which are both forms of primary instability. If a flow is perturbed at a point $x_0$, and the perturbation growth rate and velocity are such that as $t \to \infty$ the perturbation amplitude at $x_0$ decays in time, the flow is said to be convectively unstable. An example of convective instability is the growth of Tollmein–Schlicting waves within a laminar boundary layer. If a flow is perturbed at a point $x_0$, and the perturbation growth rate and velocity are such that as $t \to \infty$ the perturbation amplitude at $x_0$ increases in time, the flow is said to be absolutely unstable. For a review of absolute instability, see Huerre & Monkewitz (1990). Absolute instability is the mechanism by which

bluff-body vortex shedding is initiated (Hannemann & Oertel 1989) and has also been found to occur in free shear layers (Huerre & Monkewitz 1985). Absolute instability can be detected by linear stability methods; however transition prediction methods used in industry, for example the $e^N$ method as used in XFoil (Drela & Giles 1987), typically only consider convective stability. More recently, transition prediction by linear stability analysis of velocity profiles has been incorporated into unsteady Reynolds-averaged Navier–Stokes methods, for the purpose of predicting aerofoil flows (e.g. Radespiel & Scholz 2007; Yuan *et al.* 2007). However absolute instability is again not yet considered. The significance of absolute instability is that it occurs independent of upstream influence and can lead to the presence of unsteady behaviour even where background disturbance levels are too small in amplitude to sustain unsteadiness via convective instability. Sandham (2008) did account for absolute instability in an unsteady viscous–inviscid interaction (VII) method, where the unsteady momentum integral equation is solved for the viscous part of the solution, by including the possibility that the transition process may 'self-sustain' in a fashion similar to the behaviour observed by Jones, Sandberg & Sandham (2008).It is interesting to note however that although absolute instability has been observed for analytically constructed velocity profiles (Hammond & Redekopp 1998) and artificially generated separation bubble flows (Hammond & Redekopp 1998; Marquillie & Ehrenstein 2003), it has not yet been detected for separation bubbles naturally occurring on an aerofoil or flat plate.

Primary instability growth is therefore well understood, and accurate tools exist for its prediction. The final stages of transition are of interest but are not as important in terms of predicting the presence and location of transition. The receptivity process is less well understood and represents an important process in the prediction of transition. A review of the receptivity process may be found in Saric, Reed & Kerschen (2002). Here we will consider the idealized case of the flow over a semi-infinite flat plate with a rounded leading edge. Sufficiently far downstream of the leading edge, fluid flow within the boundary layer is approximately parallel, and the behaviour of hydrodynamic instabilities is described by the Orr–Sommerfeld equation (Schmid *et al.* 2002). In the vicinity of the leading edge, where the boundary layer thickness increases rapidly and the flow is therefore highly non-parallel, the flow is governed by the linearized unsteady boundary layer equation (Goldstein 1983). Lam & Rott (1960) constructed a set of asymptotic eigensolutions to the unsteady boundary layer equation subject to a low-amplitude disturbance field convecting with free-stream velocity. The Lam–Rott eigensolutions describe disturbance waves that decay exponentially with increasing distance and have a wavelength that decreases with increasing $x$. Hence at some streamwise location the spatial scale of the Lam–Rott disturbances will be comparable to the boundary layer thickness, at which point the approximations necessary to construct the Lam–Rott eigensolutions are no longer valid. Goldstein (1983) showed that there is a region in which the Orr–Sommerfeld normal-mode disturbances match the Lam–Rott asymptotic eigensolutions and hence may be considered natural continuations of these disturbances into the downstream region. Effectively the Lam–Rott eigensolutions describe the manner in which large-wavelength disturbances travelling at free-stream velocity can excite short-wavelength disturbances convecting within the aerofoil boundary layer. The complete receptivity process is therefore as follows. Long-wavelength disturbances in the free stream excite Lam–Rott disturbances in the vicinity of the aerofoil leading edge, which decrease in both wavelength and amplitude with increasing streamwise location, until

a sufficiently small wavelength is achieved such that they can effectively continue as Orr–Sommerfeld disturbances. As well as determining the initial amplitude of primary instabilities, the receptivity process plays an important role in the development of acoustic-feedback loops, such as those observed for cavity flow (Rossiter 1964) and separated regions formed on aerofoils (McAlpine, Nash & Lowson 1999; Desquesnes, Terracol & Sagaut 2007), and may influence the frequency selection of such 'global' instabilities. Furthermore, it is feasible that global instabilities involving feedback loops may result in transition to turbulence in the absence of explicitly added disturbances. For example, in a direct numerical simulation (DNS) of the flow around an NACA-0012 aerofoil, Deng, Jiang & Liu (2007) suggested that the transition to turbulence observed is triggered by receptivity of the boundary layer to acoustic waves originating in the wake.

It is apparent that understanding of the transition process is critical for the accurate prediction of low-Reynolds-numbers flows. The process of primary instability growth is important in determining the presence and location of receptivity and is comparatively well understood, particularly for the case of convective instability growth. Absolute instability characteristics are typically not considered when performing aerofoil flow predictions in industry, but despite this the presence of absolute instability can dramatically alter the fluid dynamics, and hence the aerodynamic performance, associated with a lifting body. The receptivity process is less understood than the primary instability process, yet it plays an important role in the transition process. Furthermore, receptivity of boundary layers to free-stream disturbances is a crucial stage in global instability mechanisms, involving acoustic-feedback loops, and must be considered if the stability of a base flow is to be fully investigated. The goal of the current study is therefore to investigate the time-averaged two- and three-dimensional flows around an NACA-0012 aerofoil at incidence in terms of both their convective and absolute stability characteristics, as well as the dependency of the acoustic receptivity process upon frequency and source location. DNSs of both the two- and three-dimensional flows around an NACA-0012 aerofoil with a laminar separation bubble have previously been conducted, at $Re_c = 5 \times 10^4$, $M = 0.4$ and $\alpha = 5°$; the simulations are discussed in detail in Jones (2007) and Jones, Sandberg & Sandham (2008). In Jones *et al.* (2008) no regions of absolute instability were observed for the time-averaged aerofoil flow with separation bubble, as determined via linear stability analysis. However the unsteady two-dimensional flow, exhibiting periodic vortex shedding from a laminar separation bubble, was found to be absolutely unstable to three-dimensional perturbations. Specifically the two- and three-dimensional time-averaged flows investigated here are those obtained from 'case two-dimensional' and 'case 3DU' respectively as referred to in Jones *et al.* (2008).

The structure of the current study is as follows. In the next section the methods used to investigate the stability of the reference flows will be outlined, detailing both the governing equations and the numerical methods employed to solve them. Numerical methods for detecting absolute instability are then applied to a test case known to exhibit absolute instability, in order to illustrate their applicability to time-averaged flows. The reference flow fields which are the focus of the current study will then be described and analysed in terms of their convective and absolute stability characteristics by means of both classical linear stability analysis and DNS. Finally, the receptivity of the reference flow to free-stream acoustic disturbances will be investigated, which, as will be illustrated, has a crucial bearing on the stability of the reference flow.

## 2. Numerical methods

The numerical method for DNS from which the reference base flows are extracted is discussed in detail in Jones *et al.* (2008); so only a concise summary is included here. Methods used to investigate the stability of the reference flows include performing DNS with forcing terms and linear stability analysis of time-averaged velocity profiles.

### 2.1. *Direct numerical simulations*

The code directly solves the unsteady compressible Navier–Stokes equations, assuming a Newtonian fluid and a Fourier law of heat conduction, which may be written in concise notation as

$$\frac{\partial \boldsymbol{Q}}{\partial t} + \frac{\partial \boldsymbol{F}}{\partial \xi} + \frac{\partial \boldsymbol{G}}{\partial \eta} = \boldsymbol{A}, \tag{2.1}$$

where $\boldsymbol{Q}$ is a vector of the conservative variables; $\boldsymbol{F}$ and $\boldsymbol{G}$ are fluxes in the $\xi$ and $\eta$ directions respectively; and $\boldsymbol{A}$ is a forcing term defined later (§§ 2.1.1 and 2.1.2). The formulation of the Navier–Stokes equations is given in Jones *et al.* (2008). The density $\rho$, velocity components $u$, $v$ and temperature $T$ have been non-dimensionalized by the free-stream conditions and the aerofoil chord is used as the reference length scale. Viscosity is calculated using Sutherland's law (White 1991), and a perfect gas is assumed. Baseline dimensionless parameters are specified as Reynolds number $Re = 5 \times 10^4$, Prandtl number $Pr = 0.72$ and Mach number $M = 0.4$. The ratio of specific heats is specified as $\gamma = 1.4$. Where frequencies are given, they are effectively normalized by the free-stream velocity and aerofoil chord and hence are equivalent to a Strouhal number defined using these quantities.

Fourth-order accurate central differences utilizing a five-point stencil are used for the spatial discretization. Fourth-order accuracy is extended to the domain boundaries by the use of a Carpenter boundary scheme (Carpenter, Nordström & Gottlieb 1999). No artificial viscosity or filtering is used. Instead, stability is enhanced by appropriate treatment of the viscous terms in combination with entropy splitting of the inviscid flux terms (Yee, Sandham & Djomehri 1999; Sandham, Li & Yee 2003). The explicit fourth-order accurate Runge–Kutta scheme is used for time stepping.

The code is based upon an existing solver that has been previously validated for compressible turbulent plane channel flow (Sandham *et al.* 2003) and more recently has been demonstrated to accurately represent the development of hydrodynamic instabilities (Sandberg, Sandham & Joseph 2007). The code used in the current study is different in that it is applied to a curvilinear C-type grid with wake connection; however the same metric terms were used in previous versions of the code (Sandberg & Sandham 2008; Sandberg *et al.* 2009).

### 2.1.1. *Hydrodynamic forcing*

Volume forcing is applied to the $x$ and $y$ momentum equations in certain simulations, by setting $\boldsymbol{A} = f(t)$, in order to introduce time-periodic disturbances that convectively are amplified in the aerofoil boundary layer, thus enabling instability growth rates to be determined. Forcing is applied about the location $(x, y) = (0.025, 0.129)$, corresponding to a point within the boundary layer of the time-averaged two-dimensional flow field, and is periodic in time. A cosine function is used to smoothly ramp the forcing terms from a maximum at the centre of the forcing location to zero at radius $5 \times 10^{-3}$ from the forcing location. Effectively, $\boldsymbol{A}$ is non-zero within this region only. The maximum amplitude of velocity disturbances introduced by the forcing is approximately $5 \times 10^{-8}$ of the free-stream velocity.

### 2.1.2. *Acoustic forcing*

For some cases a time-dependent forcing function $A$ is added to the right-hand side of the continuity equation, the goal being for the forcing location to act as an acoustic source. A cosine function is used to smoothly ramp the forcing terms from a maximum at the centre of the forcing location to zero at the edge of the forcing region, and $A$ is non-zero only within this region. Further details of the acoustic forcing are given in §6.2. The amplitude of velocity disturbances introduced by the forcing is a maximum of $1 \times 10^{-8}$ of the free-stream velocity.

## 2.2. *Classical linear stability analysis*

The stability of time-averaged velocity profiles is investigated by solving the Orr–Sommerfeld equation and is denoted 'classical' linear stability analysis. This analysis is performed by using an incompressible Orr–Sommerfeld solver in conjunction with an iterative algorithm in order to solve the spatial problem. To detect absolute stability analysis the cusp-map method is used.

### 2.2.1. *Governing equations*

For incompressible flow, boundary layer disturbances are assumed to take the form of two-dimensional travelling waves such that

$$u'_i = \hat{u}_i(y)e^{i(\alpha x - \omega t)}. \tag{2.2}$$

The variable $\alpha$ is the complex wavenumber (defined as $\alpha = 2\pi/\lambda$, where $\lambda$ is the disturbance wavelength), and $\omega$ is the complex frequency of the travelling wave (defined as $\omega = 2\pi f$, where $f$ is the disturbance frequency). Wall normal variation is accounted for in the function $\hat{u}_i(y)$, and the phase velocity is given by $c_{ph} = \omega/\alpha$. The amplitude of instability waves varies as

$$e^{\omega_i t - \alpha_i x}, \tag{2.3}$$

found by expanding (2.2); hence the imaginary part of the wavenumber $(-\alpha_i)$ corresponds to the spatial growth rate, and the imaginary part of the frequency $(\omega_i)$ corresponds to the temporal growth rate.

Assuming a parallel base flow, for which $\bar{u} = \bar{u}(y)$, $\bar{v} = 0$, $d\bar{u}/dx = 0$, the response of the boundary layer to small-amplitude perturbations of the form given by (2.2) may then be calculated by solving the Orr–Sommerfeld equation,

$$(\bar{u} - c_{ph})\left(\frac{d^2\hat{v}}{dy^2} - \alpha^2\hat{v}\right) - \frac{d^2\bar{u}}{dy^2}\hat{v} = -\frac{i\nu}{\alpha}\left(\alpha^4\hat{v} - 2\alpha^2\frac{d^2\hat{v}}{dy^2} + \frac{d^4\hat{v}}{dy^4}\right), \tag{2.4}$$

for which a full derivation is given in Drazin & Reed (1981). To solve the this equation, a velocity profile $\bar{u} = \bar{u}(y)$ is specified (extracted from time-averaged DNS data); hence $\bar{u}(y)$ and $d^2\bar{u}/dy^2$ are known. The Orr–Sommerfeld equation then represents an eigenvalue problem in matrix form $[A]\hat{v} = [B]\hat{v}$, with $\hat{v}$ as the eigenvector, which yields non-trivial solutions only for certain values of $\alpha$ and $c_{ph} = \omega/\alpha$. The eigenvalue problem may be solved in two ways, either by specifying $\alpha$ and solving for $\omega$, denoted temporal analysis, or by specifying $\omega$ and solving for $\alpha$, denoted spatial analysis.

### 2.2.2. *Numerical method*

The Orr–Sommerfeld solver used for the current study solves the temporal eigenvalue problem, returning $\omega$ for the most unstable eigenmode present. Derivatives are computed using sixth-order compact difference stencils (Lele 1992). Sufficient

resolution for the derivative scheme is indicated by smooth derivatives of velocity profiles, up to and including the fourth derivative.

In the present study velocity profiles $\bar{u}(y)$ are extracted from time-averaged DNS data. Grid requirements for DNS are typically different from those of linear stability analysis; therefore in order to avoid unnecessary computational cost, data from the DNS are interpolated on to a new grid, using cubic splines. Grids used for linear stability analysis are described by the equation

$$y_j = y_{j-1} + a(1 + s)^{j-2}, \tag{2.5}$$

for $2 < j < N$, where $N$ is the total number of grid points and

$$y_1 = 0. \tag{2.6}$$

The constant $s$ is the fractional increase in the size of successive cells, and $a$ determines the cell size at $y = 0$. In all cases the number of grid points was specified as $N = 200$, in conjunction with values $s = 5.5 \times 10^{-2}$ and $a = 1.30 \times 10^{-4}$. The grids used for the stability analysis extend further into the free stream than the grid used for DNS; hence at the domain boundary the velocity profile was smoothly ramped to free-stream conditions. The most unstable eigenmode for a Blasius boundary layer profile at $Re_{\delta^*} = 1500$, $\alpha = 0.2$ was determined, and the resultant value for $\alpha$ was found to agree with the results of Gaster (1978) up to and including the fifth digit for the real part and the sixth digit for the imaginary part.

In order to solve the spatial eigenvalue problem, which is more relevant in the current case, an iterative algorithm is employed based on the secant method. Effectively a real $\omega = \omega_{in}$ is specified, and the Orr–Sommerfeld solver is repeatedly solved within an iterative loop to find the corresponding complex $\alpha_{out}$ such that when the temporal eigenvalue is solved for $\alpha_{out}$, $\omega_{in}$ is returned to a user-specified degree of accuracy. The method is explained fully in Jones (2007).

Solving the spatial eigenvalue problem returns $\alpha$, for which $-\alpha_i$ is the exponential spatial growth rate of instability waves. This enables the wave amplitude as a function of $x$ to be computed. Given an initial disturbance amplitude $A_0$ and a disturbance amplitude $A$ at an arbitrary downstream location, the disturbance $N$-factor is defined as $N = \ln(A/A_0)$. Hence $\mathrm{d}N/\mathrm{d}x = -\alpha_i$. The $N$-factor is integrated using a Euler scheme, as

$$N(x + \Delta x) = N(x) - \alpha_i \Delta x. \tag{2.7}$$

### 2.2.3. *Cusp-map method*

In order to determine whether regions of absolute instability are present in a given flow the cusp-map method is employed. The cusp-map method is essentially a method for detecting instability waves with zero group velocity, i.e. $c_g = \delta\omega/\delta\alpha = 0$, by repeatedly solving an appropriate dispersion relation (in this case the temporal Orr–Sommerfeld equation) for a given velocity profile. Where an instability wave with zero group velocity exists, the sign of $\omega_i$ associated with the instability wave determines its absolute instability characteristics. If $\omega_i < 0$ the wave is decaying in time. If $\omega_i > 0$ the wave is increasing in amplitude with time, and hence the velocity profile is absolutely unstable. The method is the temporal equivalent of Briggs method. For a full description of both Briggs method and the cusp-map method, see Schmid et al. (2002). A brief summary is also given in Jones et al. (2008).

### 2.3. *Forced Navier–Stokes equations*

Both the absolute and convective stability characteristics of a given time-averaged reference flow can be investigated by employing DNS with forcing terms.

If a time-averaged flow field extracted from an unsteady flow were used as the initial condition for a simulation, and the simulation progressed in time, the flow field would ultimately become unsteady. In order to prevent this, forcing terms are added to the Navier–Stokes equations such that an initial condition can be maintained. The behaviour of small hydrodynamic or acoustic perturbations on the initial condition (i.e. the time-averaged flow field) can then be determined. The method is equivalent to a two-dimensional linear stability analysis, and will be referred to as such henceforth, and is not restricted to parallel flows.

A flow field of interest is assumed to be known. At the start of the simulation the temporal derivative of the conservative variable vector $Q$ is computed from the time-averaged flow variables. The simulation is then progressed, and whenever temporal derivatives are computed the stored forcing term is subtracted:

$$\frac{\partial Q}{\partial t} + \frac{\partial F}{\partial \xi} + \frac{\partial G}{\partial \eta} = \left( \frac{\partial F}{\partial \xi} + \frac{\partial G}{\partial \eta} \right)_{t=0}. \tag{2.8}$$

The result is that assuming there is no change or perturbation to the flow field, the initial condition can be maintained as a reference state, upon which the behaviour of small perturbations can be investigated. Although DNS with forcing terms are more computationally expensive than classical linear stability analysis, the method is subject to less restrictive assumptions; in particular the method is not restricted to parallel flows.

### 2.4. *A test case: aerofoil wake at $Re_c = 10^4$*

The forced Navier–Stokes and classical linear stability analysis methods have been applied to a test case with known absolute stability characteristics, in order to determine whether these methods can detect absolute instability. The chosen test case is the two-dimensional wake behind an NACA-0012 aerofoil.

A DNS has been conducted at $Re_c = 10^4$, $M = 0.2$ and $\alpha = 0°$ (Jones 2007). When the simulation is progressed, the wake exhibits roll-up into periodic von-Kárman vortex shedding downstream of the aerofoil (figure 1*a*). Adding a symmetry condition ($v = 0$) to the wake dividing line and progressing the simulation suppresses the vortex-shedding behaviour, resulting in a steady solution (figure 1*b*).

The onset of wake unsteadiness can be investigated by removing the symmetry condition and progressing the simulation. The behaviour immediately after removing the symmetry condition is monitored by recording time-dependent pressure at a number of streamwise locations in the wake. Figure 2 shows the variation of $dp/dt$ with distance, downstream of the aerofoil trailing edge, $x - x_{te}$, in the form of an $x/t$ plot. Immediately after the symmetry condition is removed, pressure oscillations are observed to initiate and grow in amplitude in the region $0.5 < x/c < 1$ downstream of the trailing edge (figure 2*a*). The very sudden localized onset and growth of this oscillation suggests that the wake is absolutely unstable at some location in the region $0 < x \leqslant 0.5$ chords downstream of the trailing edge, since the oscillation is growing temporally and does not appear to originate from an upstream location. After a short period of time pressure oscillations are observed at all points in the wake downstream of the trailing edge, and the amplitude of oscillation appears increases with downstream distance from the trailing edge (figure 2*b*). The
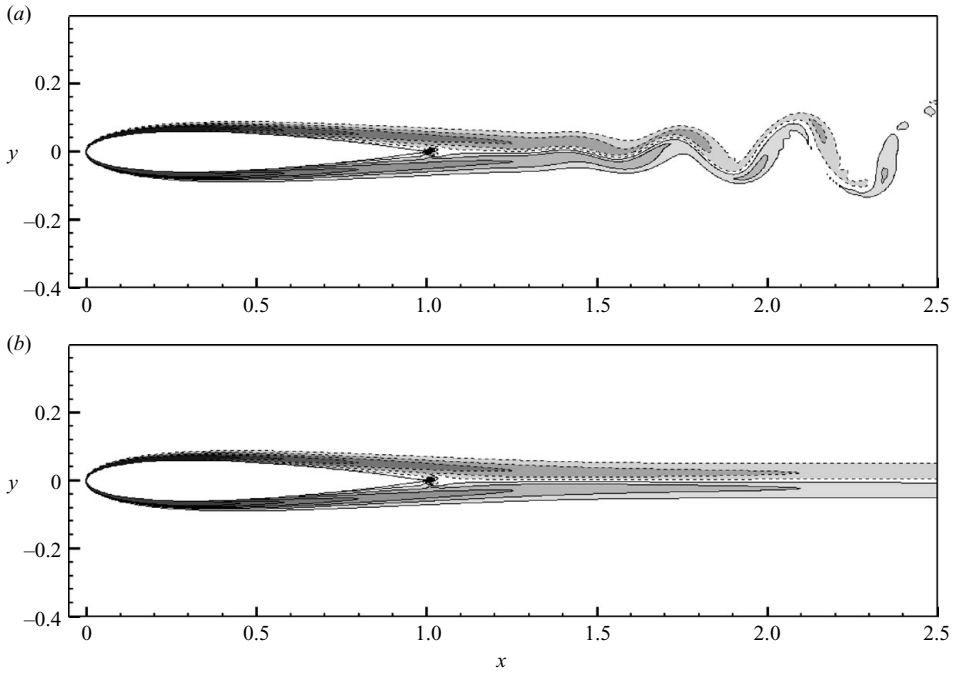
FIGURE 1. Isocontours of vorticity for the case (a) $Re_c = 10^4$, $M = 0.2$, $\alpha = 0°$ and (b) with the $v = 0$ condition applied to the wake dividing line, using 12 levels over the range $\pm 50$, with the negative contours represented as the dashed lines.
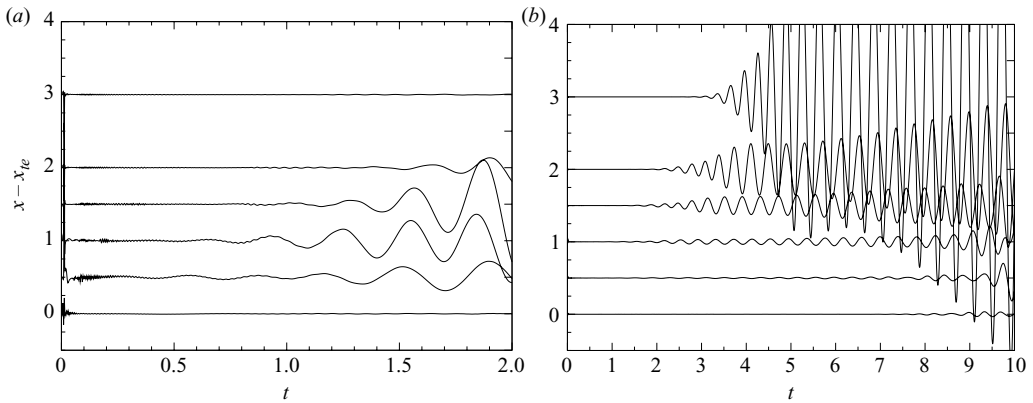


FIGURE 2. Derivative of pressure with respect to time, after the symmetry condition was removed at $t = 0$. Distance of the measurement location downstream of the trailing edge is given on the $x$-axis of (a). (a) Illustrates the behaviour immediately after the symmetry condition was released; (b) illustrates quasi-linear behaviour over a longer period of time.

fact that the amplitude of oscillation increases with downstream location suggests that the wake is also convectively unstable. Oscillations are observed to grow in amplitude exponentially until nonlinearity occurs (figure 3), ultimately leading to vortex shedding.
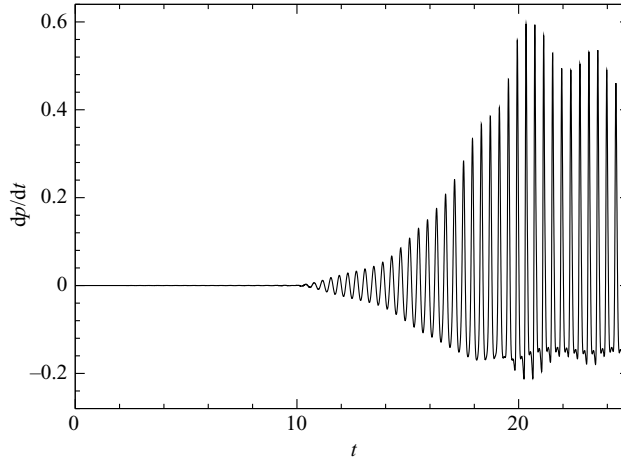
FIGURE 3. Derivative of time-dependent pressure with respect to time recorded one chord downstream of the aerofoil trailing edge.
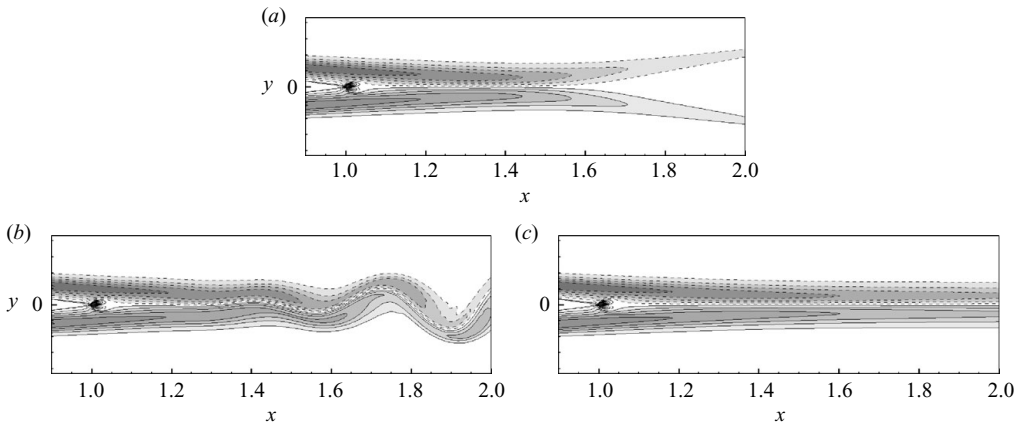


FIGURE 4. Isocontours of vorticity using 20 levels over the range $\pm 50$ for the (*a*) time-averaged flow field, (*b*) instantaneous flow field and (*c*) symmetrized flow field for a case at $Re_c = 10^4$, $M = 0.2$, $\alpha = 0°$, with the negative contours represented as the dashed lines.

### 2.4.1. *Cusp-map method*

Velocity profiles extracted from the simulation at $Re_c = 10^4$ were analysed using the cusp-map method in order to confirm that the method is capable of detecting absolute instability. Three flow fields were investigated: the symmetrized flow field, the time-averaged non-symmetrized flow field and the instantaneous flow field (illustrated in figure 4). The complex $\alpha$-plane was swept with a minimum resolution of $\Delta \alpha_r = \Delta \alpha_i = 2$. The corresponding resolution in the complex $\omega$-plane is much higher in the vicinity of a branch point, since $\partial \omega / \partial \alpha \approx 0$. Branch-point singularities associated with zero-group-velocity instability waves have been tracked, traversing the wake over the region 0.01–0.5 chords downstream of the aerofoil trailing edge. Imaginary parts of the complex frequency associated with $c_g = 0$ are plotted in figure 5. For all cases, at 0.01 chords downstream of the trailing edge the $c_g = 0$ wave is growing temporally, i.e. $\omega_i > 0$, and hence the flow is absolutely unstable. The temporal growth rate decreases
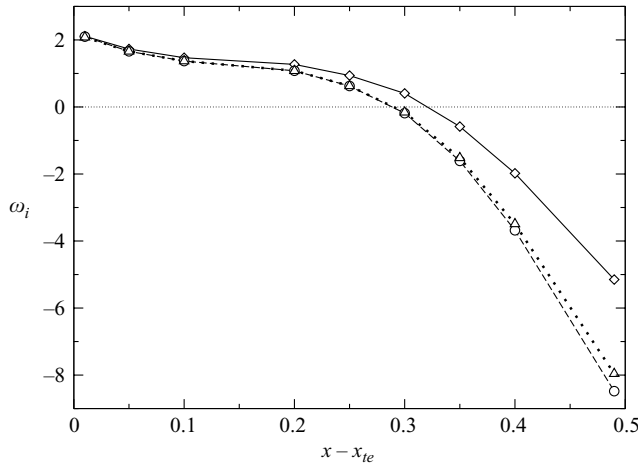
FIGURE 5. Variation with $x$ of $\omega_i$ associated with $c_g = 0$, for the case $Re_c = 10^4$, $M = 0.2$, $\alpha = 0°$, with the $x$-axis showing the distance downstream from the aerofoil trailing edge, showing results for the time-averaged flow field ($\bigcirc - -\bigcirc$), instantaneous flow field ($\triangle \cdots \triangle$) and the flow field with symmetry condition applied ($\diamond\!-\!\diamond$).

with increasing $x$ and at approximately 0.3 chords downstream of the trailing edge $\omega_i = 0$; hence the flow transitions from absolutely unstable to convectively unstable. As $x$ increases to 0.5 chords downstream of the trailing edge, $\omega_i$ decreases further. The cusp-map method clearly detects absolute instability in the near-wake region for all three cases. Results for the instantaneous and time-averaged flow fields are similar; however the symmetrized flow field exhibits a greater tendency towards absolute instability (i.e. $\omega_i$ is greater). This trend agrees with the work of Barkley (2006), who, for the case of bluff-body shedding, determined that stability analysis of the time-averaged flow exhibits reduced growth rates as compared with that of a symmetrized 'base flow'.

### 2.4.2. *Two-dimensional linear stability analysis*

A direct numerical simulation of the symmetrized aerofoil wake at $Re_c = 10^4$ has been performed, employing forcing terms to maintain the initial condition as detailed in §2.3. The behaviour of small perturbations on the initial condition, i.e. the symmetrized flow field, can then be determined in order to confirm that the method is able to detect absolute instability.

A region of $3 \times 3$ grid points about the location $(x, y) = (1.00, 0.05)$, corresponding to a location within the upper surface boundary layer at the trailing edge, is subject to an increment of $1 \times 10^{-8}$ in $u, v$ and $\rho$. This introduces a disturbance with a sharp-edged spatial distribution, which will excite a range of wavenumbers (and hence frequencies) at low amplitude. No further perturbations are introduced, and the response of the flow is monitored as the simulation is progressed. If the flow were only convectively unstable, the initial perturbation would be expected to convect downstream whilst growing in amplitude, ultimately leaving the flow over the aerofoil unperturbed. If the flow were absolutely unstable, the initial perturbation would be expected to grow exponentially in time at some location until saturation or the onset of some secondary behaviour, ultimately affecting the entire flow field.

The response of the flow field is monitored in two ways: by recording the time-dependent pressure at several $x$-locations within the wake and by analysing the
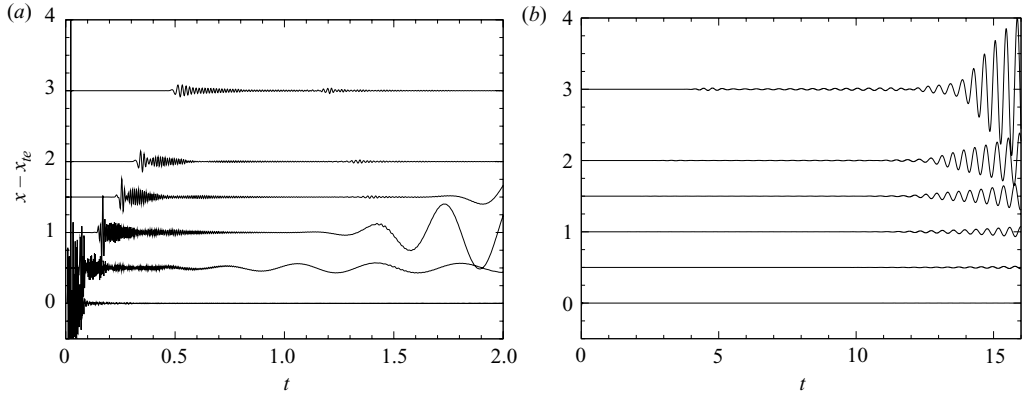
FIGURE 6. Time histories of $dp/dt$, with streamwise distance from the aerofoil trailing edge indicated on the vertical axis, for time (*a*) $0 < t < 2$ and (*b*) $0 < t < 16$.

contour plots of flow field quantities. If post-processed quantities were plotted for the instantaneous flow field, the perturbation and its subsequent response would not be visible. This is because variations in the mean flow field are much larger in magnitude than those caused by the perturbation. In order to better visualize perturbations to the mean field, isocontours of the perturbation $z$-vorticity rate are plotted, defined as $\omega_z' = \omega_{zt=t_1} - \omega_{zt=0}$, where $\omega_{zt=t_1}$ is the $z$-vorticity at time $t_1$ and $\omega_{zt=0}$ is the $z$-vorticity at time $t = 0$.

Figure 6 shows time series of $dp/dt$ taken at several streamwise locations within the aerofoil wake. Time $t = 0$ is the initialization time, at which the perturbation was introduced. Signals are plotted at an arbitrary amplitude; however all signals were scaled by the same factor. Considering first the interval $0 < t < 2$ (figure 6*a*), pressure fluctuations are observed almost immediately at 0.5 chords downstream of the trailing edge. The amplitude of unsteadiness increases at one chord downstream of the trailing edge; however the onset of unsteadiness occurs at a later time. When plotted for the interval $0 < t < 16$ (figure 6*b*) the pressure fluctuations are observed to increase in amplitude temporally, in an exponential fashion, at all locations downstream of the trailing edge. The amplitude of pressure fluctuations also increases with distance from the trailing edge. No unsteadiness is observed in the boundary layer directly at the trailing edge when plotted at these levels. The behaviour observed in figure 6(*a*) is similar to that observed in figure 3, where the onset of unsteadiness from the symmetrized wake was observed. Isocontours of $\omega_z'$ (figure 7) reveal that these fluctuations are associated with a vorticity perturbation that is oscillatory in $x$ and symmetric about the wake centreline. The associated $u$-velocity perturbation would be antisymmetric about the wake centreline.

This behaviour confirms that a region of absolute instability is present in the region $0 < x \leqslant 0.5$ chords downstream of the trailing edge. It appears that unsteadiness is generated in the region $0 < x \leqslant 0.5$ chords downstream of the trailing edge via absolute instability. Downstream of this location the perturbations are subsequently convectively amplified, ultimately leading to vortex shedding.

Both the cusp-map method and the forced Navier–Stokes method have proven capable of detecting absolute instability for the case of the symmetrized aerofoil wake. Furthermore, the cusp-map method detected absolute instability in both the instantaneous wake and the time-averaged wake. These results appear to justify the
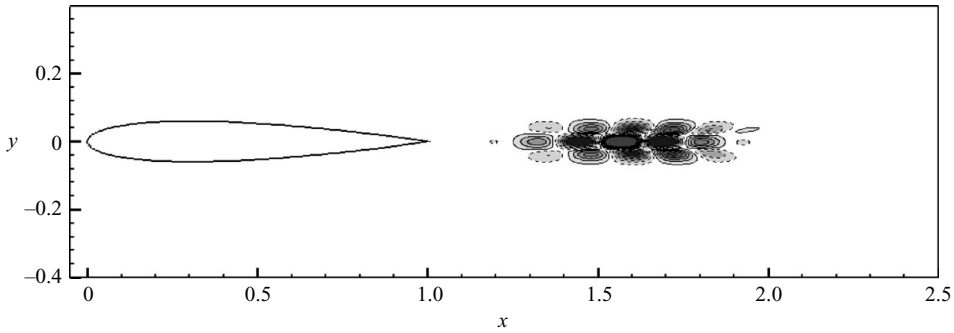
FIGURE 7. Isocontours of $\omega'_z$ for the simulation with forcing terms at $M = 0.2$, using 12 levels over the range $\pm 3 \times 10^{-8}$, with the negative contours represented as the dashed lines.
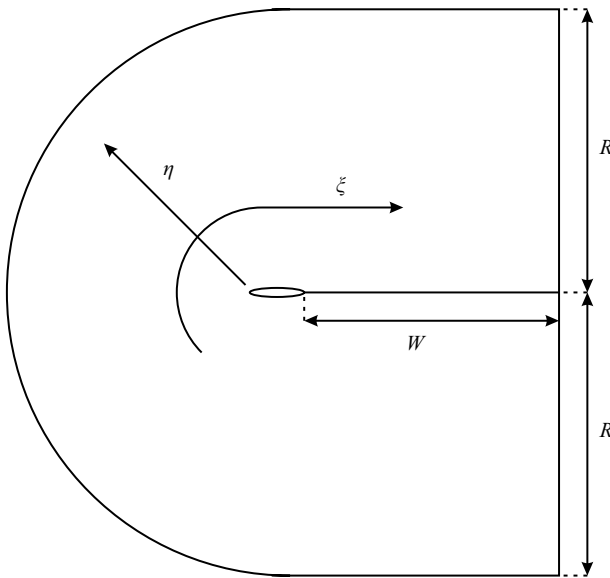


FIGURE 8. Domain topology for aerofoil DNS.

application of linear stability analysis to time-averaged flow fields for the purpose of detecting absolute instability.

## 3. The reference aerofoil flow

The aim of the current study is to investigate the convective and absolute stability characteristics of the time-averaged two- and three-dimensional flows around an NACA-0012 aerofoil at $Re_c = 5 \times 10^4$, $M = 0.4$ and $\alpha = 5°$. The simulations from which the reference (time-averaged) flow fields are extracted are discussed in detail in Jones (2007) and Jones *et al.* (2008). The topology of the curvilinear C grid used is given in figure 8, and grid parameters are given in table 1. The coordinate system is defined such that the aerofoil trailing edge is located at $(x, y) = (1, 0)$, and it should be noted that the NACA-0012 aerofoil geometry is extended to include a sharp trailing edge and rescaled to unit chord length. The three-dimensional simulation is well resolved, with the maximum grid spacing in terms of wall units being $x^+ = 3.36$,

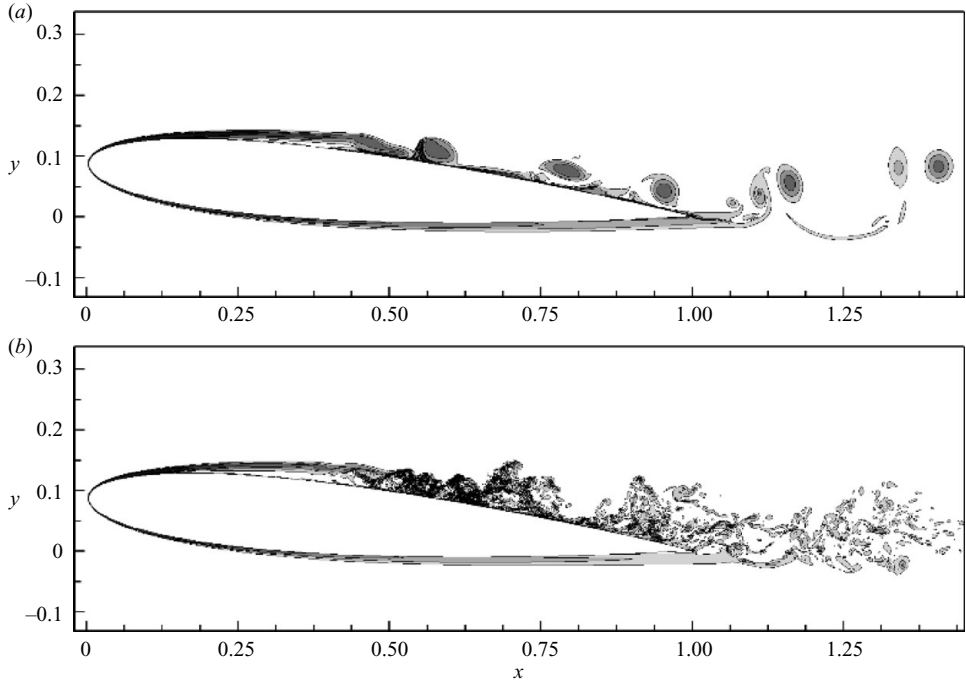| $R$ | $W$ | $L_z$ | $N_\xi$ | $N_\eta$ |
|---|---|---|---|---|
| 7.3 | 5 | 0.2 | 2570 | 691 |

TABLE 1. Domain dimensions.



FIGURE 9. Isocontours of vorticity, using 20 levels over the range $\pm 150$, at $Re_c = 5 \times 10^4$, $M = 0.4$ for the instantaneous flow fields of (*a*) the two-dimensional case and (*b*) the three-dimensional case.

$z^+ = 6.49$ and $y^+_{y=0} = 1.0$, when taken at the location of maximum skin friction within the turbulent region of the three-dimensional simulation. A brief description of the fluid dynamics of the original simulations is included here, as background to the current study.

When the simulation is run in two dimensions, the upper surface aerofoil boundary layer separates at $x = 0.151$ because of the presence of an adverse pressure gradient. The separated shear layer then rolls up into periodic vortex shedding at $x \approx 0.5$, with frequency $f = 3.37$ (figure 9*a*). Such vortex shedding is characteristic of both two- and three-dimensional separation bubble flows (Pauley, Moin & Reynolds 1990; Yang & Voke 2001), and for three-dimensional flows vortices have been observed to become more coherent with decreasing Reynolds number (Zhang, Hain & Kähler 2008). The instantaneous flow is highly unsteady; however the time-averaged flow field appears qualitatively similar to the classical bubble models (e.g. Horton 1968), with a clearly defined reverse-flow vortex and reattachment point (figure 10*a*). When the simulation is run in three dimensions, with no explicitly added disturbances, the separated shear layer undergoes transition to turbulence and reattaches as a turbulent boundary layer (figure 9*b*). The instability mechanism leading to transition is described in Jones
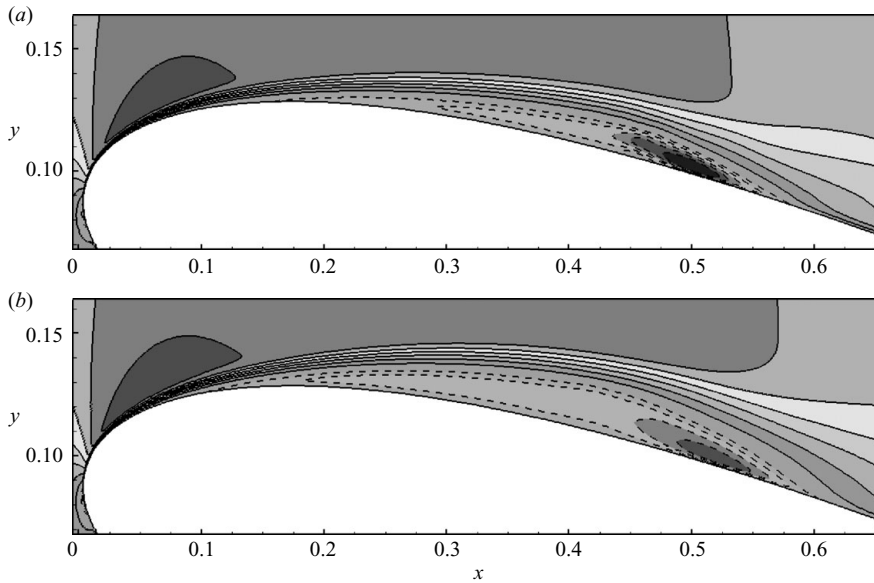
FIGURE 10. Isocontours of velocity, using 12 levels over the range $-0.2 \leqslant u \leqslant 1.4$, at $Re_c = 5 \times 10^4$, $M = 0.4$, for the time-averaged flow fields of (a) the two-dimensional case and (b) the three-dimensional case. The negative contours are shown by the dashed lines. Note that the images have been stretched in the $y$-direction to show the bubble more clearly.

*et al.* (2008), and results in turbulence that 'self-sustains'. The structure of the bubble changes in comparison with the two-dimensional case; the separation point moves upstream to $x = 0.099$, and the separated shear layer becomes thicker in terms of displacement thickness. Again, the time-averaged flow field resembles the classical bubble model (figure 10b).

## 4. Convective stability characteristics

### 4.1. *Classical stability analysis*

The convective stability characteristics of the two- and three-dimensional flow around an NACA-0012 aerofoil at $\alpha = 5°$ have been investigated by solving the spatial Orr–Sommerfeld problem (§2.2) for velocity profiles extracted from the time-averaged flow field, starting at a location near the aerofoil leading edge and marching to beyond the reattachment point in each case. At each $x$-location a range of real disturbance frequencies was specified, for which the code returns the associated complex wavenumber ($\alpha$), the imaginary part of which corresponds to the spatial growth rate of the instability wave. Assuming an initial disturbance amplitude of $A = A_0$ at $x = 0.05$, disturbances are then integrated spatially across the bubble using a Euler method, to determine an '$N$-factor' for each disturbance frequency, i.e. $\ln(A/A_0)$, where $A_0$ is the initial disturbance amplitude and $A$ is the disturbance amplitude at some point of interest. Results are summarized in figure 11, noting that although only 8 frequencies are plotted, calculations were performed for 16 frequencies in total, over the same range. Only half of the data is plotted for the sake of clarity. Images on the left display the variation of spatial growth rate, $-\alpha_i$, with $x$ and hence show how the stability of travelling waves varies. Images on the right display how the $N$-factor of instability waves varies with $x$ and frequency.
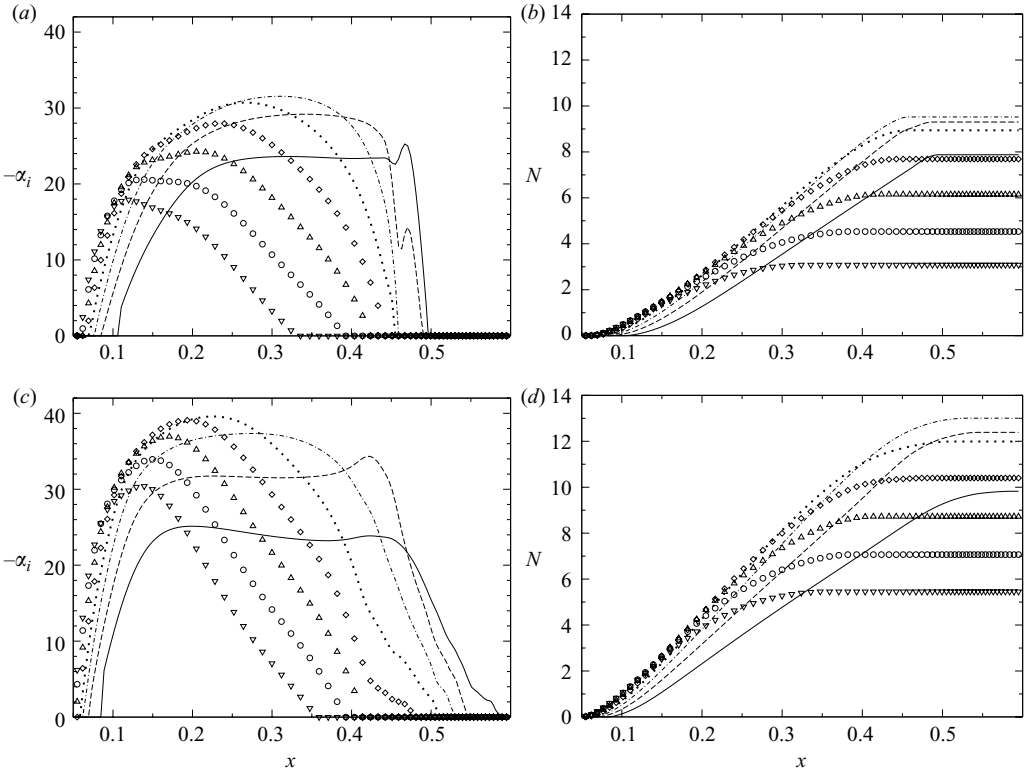
FIGURE 11. Variation of spatial growth rate with $x$ for the reference flow from ($a$) the two-dimensional simulation and ($c$) the three-dimensional simulation, and variation of the $N$-factor with $x$ for the reference flow from ($b$) the two-dimensional simulation and ($d$) the three-dimensional simulation, as computed via linear stability analysis of time-averaged velocity profiles, at frequencies $f = 4.24$ (——), $f = 6.37$ (– –), $f = 8.49$ (– ·), $f = 10.61$ (· · ·), $f = 12.73$ ($\diamond$), $f = 14.85$ ($\triangle$), $f = 16.98$ ($\circ$) and $f = 19.10$ ($\triangledown$).

The maximum spatial growth rate of instability waves computed for the time-averaged flow field of the three-dimensional DNS ($-\alpha_i \approx 40$) is significantly larger than that of the time-averaged flow field from the two-dimensional DNS ($-\alpha_i \approx 32$). This suggests that the separated region is more unstable for the three-dimensional case. The frequency of the instability wave with the largest spatial growth rate varies; for the two-dimensional case the peak growth rate occurs for frequency $f = 8.49$, whereas for the three-dimensional case the peak growth rate occurs for frequency $f = 10.61$. For all frequencies computed $\alpha_i$ is either zero or has very small amplitude for all frequencies at $x = 0.05$. This implies that $N$-factor across the bubble and the frequency of the most amplified instability wave would not change if the starting point of the stability analysis were moved further upstream. The neutral point as regards convective instability appears to be $x \approx 0.05$ for all cases. Despite variations in the frequency of the instability wave with the maximum $\alpha_i$, the frequency of the instability wave with the highest $N$-factor (i.e. the most amplified instability wave across the bubble) is approximately $f = 8.49$ ($\omega = 53.3$) for both cases.

The time-averaged flow field from the three-dimensional case exhibits a maximum $N$-factor of $N \approx 13$, whereas for the time-averaged flow field of the two-dimensional case the maximum $N$-factor is $N \approx 9.5$, confirming that the separated shear layer is
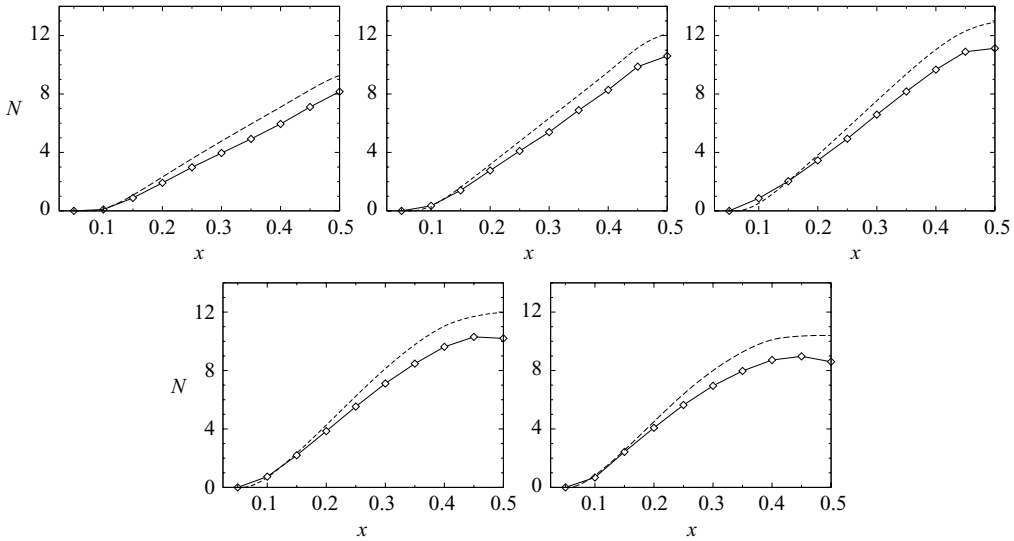
FIGURE 12. Variation of $N$-factor with $x$ for the reference flow from the three-dimensional simulation as computed by DNS ($\diamond---\diamond$) and linear stability analysis of time-averaged velocity profiles (——). From left to right, the top row of images illustrates frequencies $f = 4.24$, $f = 6.37$ and $f = 8.49$; the bottom row illustrates $f = 10.61$ and $f = 12.73$.

more convectively unstable for the three-dimensional case. An important observation is that the frequency of the greatest $N$-factor disturbance wave for the two-dimensional case at $\alpha = 5°$ ($f = 8.49$) is much higher than that of the naturally occurring vortex shedding, at $f = 3.37$. Pauley, Moin & Reynolds (1990) performed DNS of a separation bubble induced on a flat plate in two dimensions, which also exhibited naturally occurring vortex shedding, and concluded that the vortex shedding was the result of an essentially inviscid instability of the separated shear layer. Clearly this is not the case in the current study. It should be noted that for all cases, the $N$-factors observed are too small to amplify the round-off error ($\sim 1 \times 10^{-16}$) to nonlinear amplitudes ($\sim 1 \times 10^{-2}$); hence amplification of round-off error is not a possible route to transition to turbulence in the three-dimensional simulation.

### 4.2. *Two-dimensional linear stability analysis*

For comparison with the classical linear stability analysis performed in §4.1, DNS using forcing terms (§2.3) are employed to compute convective instability growth rates. The initial condition is the time-averaged flow field of the three-dimensional aerofoil simulation at $\alpha = 5°$. Forcing terms are added to the governing equations to maintain the initial condition, as explained in §2.3. Time-periodic volume forcing is applied at $x = 0.02$, introducing velocity fluctuations of the order $1 \times 10^{-8}$, which will be amplified as they convect downstream. The amplitude of pressure fluctuations is monitored at several streamwise locations in the aerofoil boundary layer, with the $y$-coordinate chosen to correspond to the location of maximum vorticity, enabling amplitude as a function of streamwise location to be plotted.

Results are plotted alongside equivalent data generated via linear stability analysis in figure 12. It is apparent that disturbance growth rates extracted from the DNS do not exactly match those computed via integrating growth rates obtained via classical linear stability analysis across the separation bubble. For all frequencies classical LST predicts an $N$-factor that is larger than that obtained via DNS, and the discrepancy
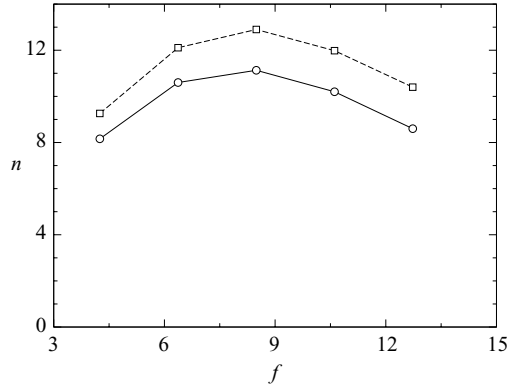
FIGURE 13. Variation of the maximum $N$-factor with frequency, showing DNS results ($\bigcirc - - \bigcirc$) and LST predictions ($\square - - \square$).
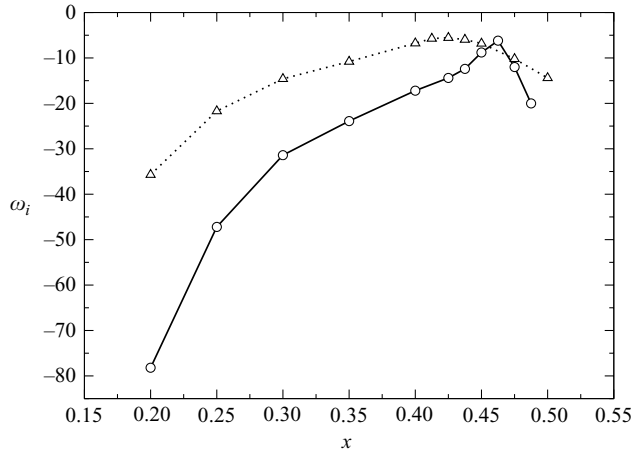


FIGURE 14. Variation with $x$ of $\omega_i$ associated with $c_g = 0$, for the reference flow from the two-dimensional case ($\bigcirc\!\!-\!\!\bigcirc$) and the reference flow from the three-dimensional case ($\triangle \cdots \triangle$) at $\alpha = 5°$.

appears to worsen with increasing frequency. It is likely that the errors are caused by non-parallel effects and that the parabolized stability equations would provide more accurate results. Despite these differences the maximum $N$-factor is observed at $f = 8.49$ for both methods. For the current case classical linear stability analysis appears to successfully describe the qualitative variation of instability growth rates with frequency, as illustrated in figure 13, and hence is still of use, e.g. when selecting unstable modes to trigger transition in numerical studies.

## 5. Absolute stability characteristics

### 5.1. *Cusp-map method*

In Jones *et al.* (2008) the time-averaged flow fields of the two- and three-dimensional simulations were investigated in terms of their absolute stability characteristics via the cusp-map method. The results are reproduced for completeness in figure 14. Singularities associated with zero-group-velocity instability waves were tracked, traversing the upper aerofoil surface from $x = 0.1$ until it was no longer possible

to locate any branch point, and imaginary parts of the complex frequency associated with $c_g = 0$ are plotted. In both cases, as the $c_g = 0$ instability wave is tracked downstream, $\omega_i$ increases with $x$, until a maximum value is reached towards the rear of the separation bubble. After reaching this maximum value, $\omega_i$ decays with further increase in $x$. For both cases, at all locations analysed, $\omega_i$ associated with the singularity is negative, and hence there is no evidence that absolute instability is present. This is consistent with Alam & Sandham (2000) for the low levels of reverse flow present. It should be noted that the location at which the strongest tendency towards absolute instability is observed (i.e. when the $c_g = 0$ wave is least damped) appears not to be the location at which the reverse flow is strongest; for both cases the location of maximum $\omega_i$ is upstream of the maximum reverse flow location.

## 5.2. *Two-dimensional linear stability analysis*

For both simulations of the case shown in figure 14 a zero-group-velocity wave could not be located downstream of a certain $x$-location, unique to that case. Downstream of this location, the Orr–Sommerfeld solver returned trivial solutions for regions of the complex $\alpha$-plane. Hence although the results suggest that $\omega_i$ associated with the $c_g = 0$ wave is decreasing with $x$ in both cases, the analysis cannot be considered a rigorous proof that no absolute instability is present.

Simulations with forcing terms are therefore conducted, via the method outlined in §2.3, in order to investigate whether any absolute instability is present that was not predicted by the cusp-map analysis. The initial condition is the time-averaged two-dimensional aerofoil flow. A region of $3 \times 3$ grid points about the location $(x, y) = (0.25, 0.136)$, corresponding to a location within the separated shear layer, is subject to an increment of $1 \times 10^{-8}$ in $u$, $v$ and $\rho$. No further perturbations are introduced, and the response of the flow is monitored as the simulation is progressed.

### 5.2.1. *Results*

The response of the flow field is monitored by recording pressure at a variety of $x$-locations within the boundary layer and analysing contour plots of flow field quantities. In order to better visualize the flow, isocontours of the perturbation dilatation rate are plotted, defined as $\nabla \cdot \boldsymbol{U}' = \nabla \cdot \boldsymbol{U}_{t_1} - \nabla \cdot \boldsymbol{U}_{t=0}$, where $\nabla \cdot \boldsymbol{U}_{t_1}$ is the dilatation rate at time $t_1$ and $\nabla \cdot \boldsymbol{U}_{t=0}$ is the dilatation rate at time $t = 0$.

Figure 15 shows time series of $\mathrm{d}p/\mathrm{d}t$ taken at several streamwise locations within the upper surface boundary layer. Time $t = 0$ is the initialization time, at which the perturbation was introduced. Signals are plotted at an arbitrary amplitude; however it should be noted that signals represented by the dashed lines are plotted at levels 50 times more sensitive than those represented by solid lines, because of the lower amplitude of the pressure signal in this region. The $x$-location of each signal is indicated on the vertical axis; hence upstream-travelling disturbances will move downwards with increasing $t$ and downstream-travelling waves will move upwards with increasing $t$. The response to the perturbation is as follows:

(i) The initial response to the perturbation can be observed by considering the time interval $0 < t < 1$; the perturbation induces a wavepacket which convects downstream towards the trailing edge. It should be noted that at no point does the wavepacket appear to trigger exponential temporal growth at a fixed $x$-location that would indicate the onset of absolute instability (e.g. compared with Hannemann & Oertel 1989 or figure 2 of the current study.

(ii) In the interval $1 < t < 2$ the original wave has convected over the aerofoil trailing edge, and no more downstream-travelling waves are observed. However the first six
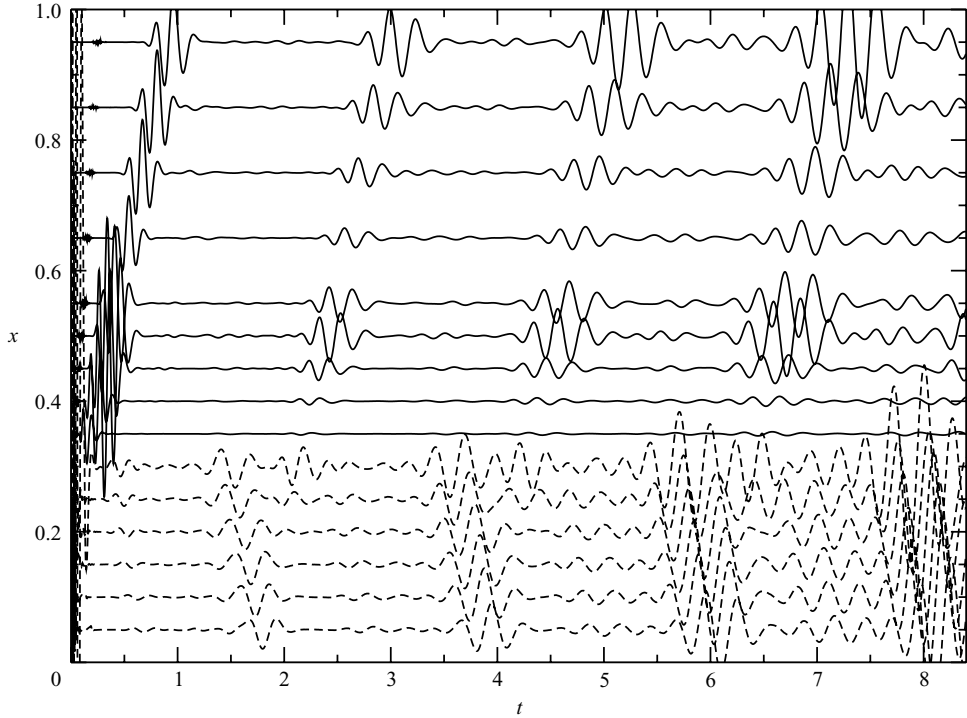
FIGURE 15. Time histories of $dp/dt$, with the streamwise location indicated on the vertical axis. The solid lines have been multiplied by $2.5 \times 10^5$ and the dashed lines by $1.25 \times 10^7$.

probes indicate that an upstream-travelling pressure wave is present, albeit at much lower amplitude, since these probes are plotted at significantly more sensitive levels.

(iii) In the interval $2 < t < 3$, after the upstream-travelling pressure wave has reached the leading edge of the aerofoil, a further downstream-travelling wave is observed. By $t = 3$ this pressure wave has reached the aerofoil trailing edge, and a new upstream-travelling pressure wave is subsequently observed.

This pattern of the downstream-travelling wave followed by the upstream-travelling wave continues, and crucially, both upstream and downstream-travelling disturbances grow in amplitude at all $x$-locations. The cause of this behaviour is illustrated by plotting the contours of $\nabla \cdot \boldsymbol{U}'$. At $t = 0.49$ (figure 16a) the wavepacket generated by the initial disturbance is visible as a multi-lobed structure. By $t = 0.98$ (figure 16b) the wavepacket has convected downstream over the trailing edge, whereupon scattering of the disturbances produces upstream-travelling acoustic waves (Ffowcs Williams & Hall 1970). The acoustic waves are more clearly visible at $t = 1.47$ (figure 16c). By $t = 2.45$ (figure 16d) another wavepacket is observed. This second wavepacket has reached the trailing edge of the aerofoil by $t = 2.94$ (figure 16e), generating more upstream-travelling acoustic waves which are clearly observed at $t = 3.43$ (figure 16f). Another wavepacket is generated at $t = 4.41$ (figure 16g), and the process continues as the amplitude of both downstream-travelling hydrodynamic structures and upstream-travelling acoustic waves increases.

From the time-series, it appears that the downstream-travelling wavepacket induced by the initial perturbation generates upstream-travelling acoustic waves when it convects over the trailing edge. These upstream-travelling acoustic waves then reach
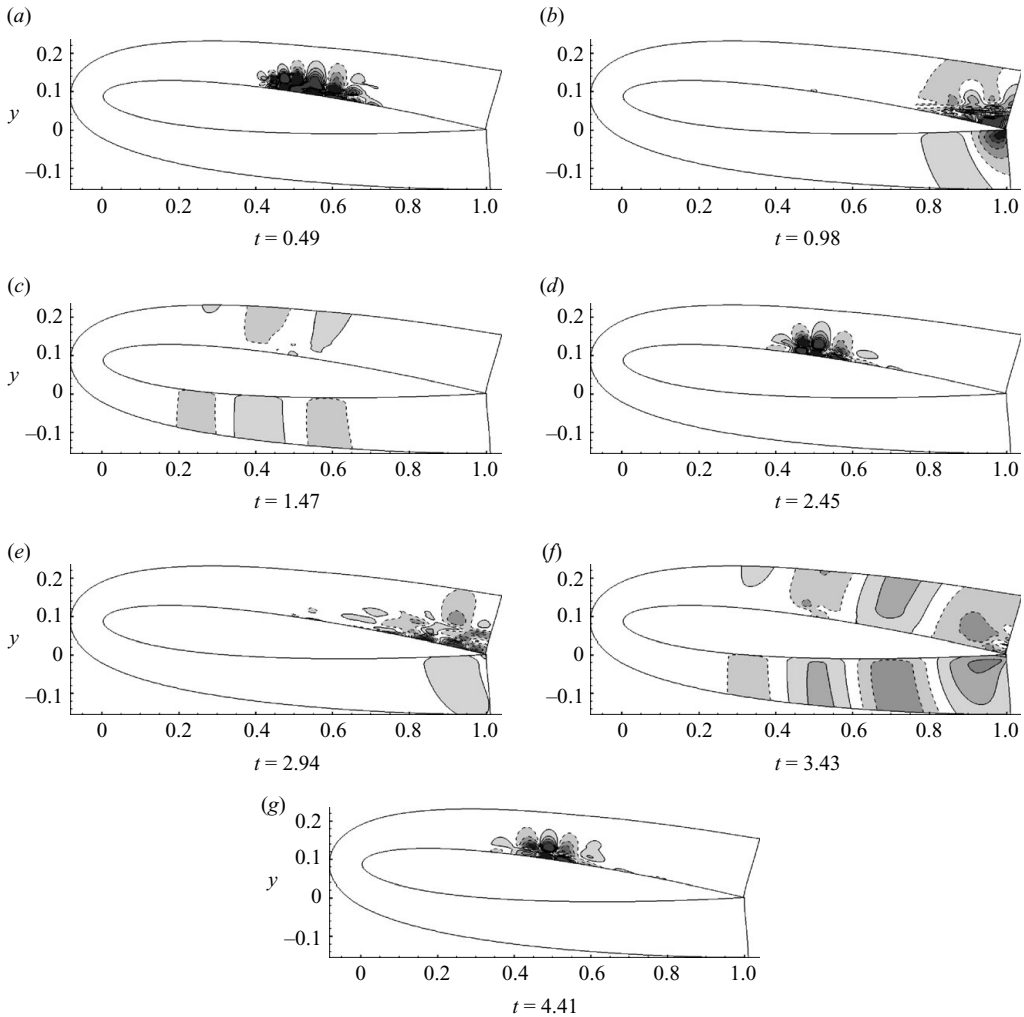
FIGURE 16. Isocontours of $\nabla \cdot \boldsymbol{U}'$ taken at the times indicated, using 10 levels over the range $\pm 10^{-8}$, with the negative contours represented as the dashed lines.

some location of receptivity, probably the aerofoil leading edge, and generate another downstream-travelling wavepacket. The process repeats with increasing amplitude at all $x$-locations and hence represents an instability of the flow, via a combination of convective instability of hydrodynamic disturbances and an acoustic-feedback loop. The growth rate of the feedback loop is observed to be exponential when longer time series of pressure signals are plotted (figure 17$a$), with growth rate $e^{0.25t}$. When absolute values are plotted on a logarithmic scale (figure 17$b$) it can be seen that initially the disturbance amplitude decays in time, before growing exponentially.

A schematic of the feedback loop is illustrated in figure 18, with the four processes involved labelled A to D. During stage A, hydrodynamic disturbances are amplified as they convect downstream. Upon reaching the aerofoil trailing edge, at stage B, upstream-travelling pressure waves are generated via acoustic scattering. The pressure waves generated at the trailing edge propagate upstream during stage C. When the pressure waves reach the vicinity of the leading edge, at stage D, further
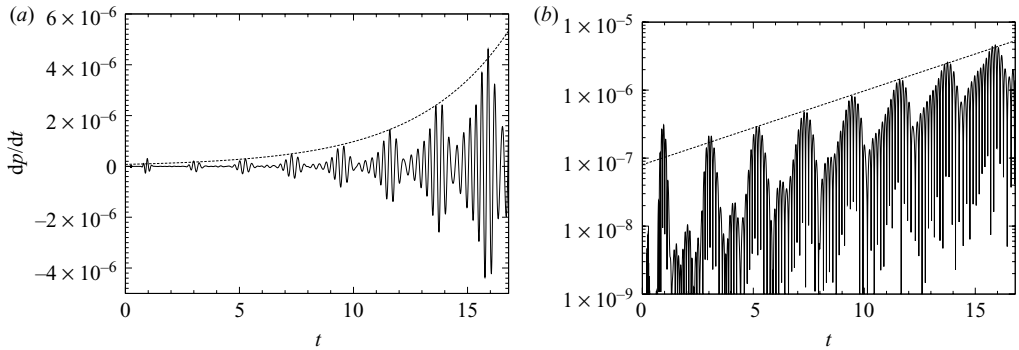
FIGURE 17. Time-dependent $dp/dt$ taken at $x = 0.95$ for the two-dimensional case at $\alpha = 5°$, (a) showing exponential disturbance growth at a rate of $e^{0.25t}$ and (b) the equivalent absolute values plotted on a logarithmic scale.
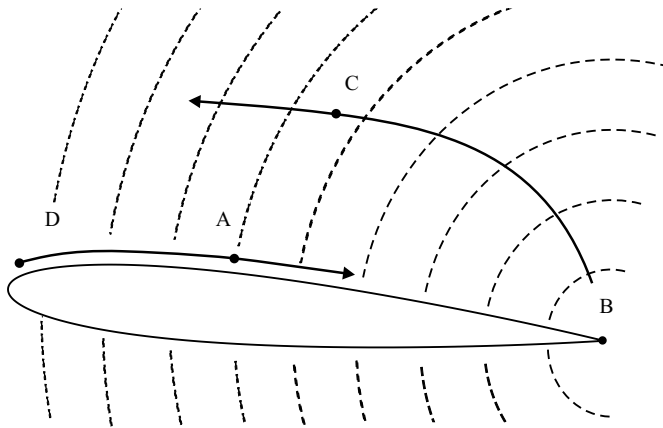


FIGURE 18. Schematic for the acoustic-feedback loop.

downstream-convecting disturbances are generated within the boundary layer, and the cycle repeats. The mechanism is analogous to Rossiter modes observed in cavity flows (Rossiter 1964), although in the current case it should be noted that the period of the feedback loop ($\Delta t \approx 2$) is distinct from, and much longer than, the period of the repeating hydrodynamic/acoustic disturbance ($\Delta t \approx 0.25$). In order for the feedback loop to be unstable, the net gain of processes A–D must be greater than 1. Process A represents the only point at which amplification takes place within the loop; hence it appears likely that strong growth of hydrodynamic instabilities is necessary to offset the losses incurred at all other stages of the cycle. Haddad, Erturk & Corke (2005) determined that the receptivity of boundary layers to acoustic disturbances (process D) increases both with aerodynamic loading and in the presence of separation; hence aerofoil incidence is expected to be a critical onset parameter for the feedback loop.

The schematic illustrated in figure 18 shares similarities with the mechanisms proposed by Desquesnes *et al.* (2007) for the generation of tonal noise observed at higher Reynolds numbers (McAlpine *et al.* 1999). For the case investigated by Desquesnes *et al.* (2007) and McAlpine *et al.* (1999) the tonal noise is produced primarily by a feedback loop involving a separated region adjacent to the trailing edge on the lower aerofoil surface, and both studies concluded that the dominant acoustic tone matches that of the most convectively amplified instability wave on
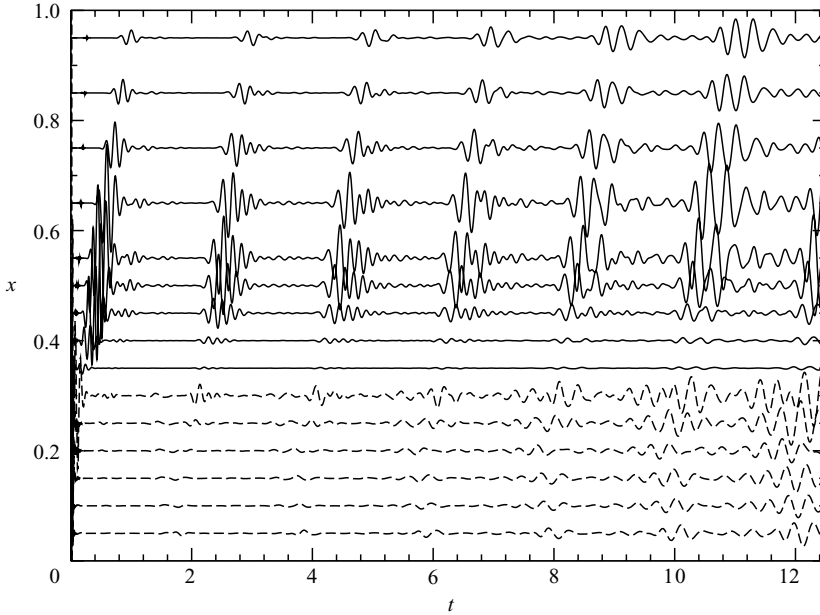
FIGURE 19. Time histories of $\mathrm{d}p/\mathrm{d}t$, with the streamwise location indicated on the vertical axis, for the three-dimensional case at $\alpha = 5°$. The solid lines have been multiplied by $1 \times 10^6$ and the dashed lines by $4 \times 10^7$.

the lower aerofoil surface. The mechanism observed in the current study is different in that the acoustic-feedback loop involves the upper aerofoil surface only and also because the dominant frequency of the acoustic-feedback loop is significantly lower than that of the most amplified instability wave.

When the process is repeated using the time-averaged flow field of the three-dimensional simulation the same behaviour is observed (figure 19), although the exponential growth rate of the instability is slightly less at $\sigma = 0.21$ as opposed to $\sigma = 0.25$. In order to make sure that no temporal disturbance growth that is independent of the acoustic-feedback loop is present, a further simulation was run. The time-averaged flow field from the two-dimensional simulation at $\alpha = 5°$ was again used as the initial condition, and the simulation was perturbed in exactly the same way, but this time a weak buffer was applied over the aft section of the aerofoil in order to damp any fluctuation present in this region.

The buffer ramps the conservative variables to the initial condition over the range $0.65 < x < 1$, modifying the conservative variables in the following fashion:

$$\boldsymbol{Q}' = \boldsymbol{Q} + \frac{1}{2}\beta \left[ 1 - \cos \left( \pi \frac{x - x_{start}}{x_{end} - x_{start}} \right) \right] (\boldsymbol{Q}_{store} - \boldsymbol{Q}), \tag{5.1}$$

where $\boldsymbol{Q}_{store}$ is the initial value of the conservative variables; $x_{start}$ is the streamwise buffer onset; $x_{end}$ is the end of the ramping function; and $\beta = 0.05$ is a constant. For $x < x_{start}$ the conservative variables are not modified, whereas for $x > x_{end}$ the conservative variables are modified as

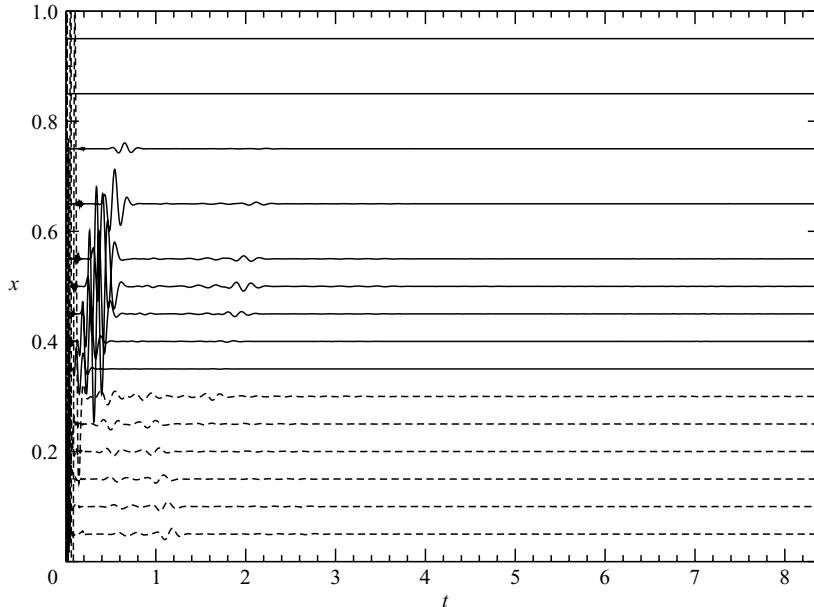$$\boldsymbol{Q}' = \boldsymbol{Q} + \frac{1}{2}\beta (\boldsymbol{Q}_{store} - \boldsymbol{Q}). \tag{5.2}$$

FIGURE 20. Time histories of $dp/dt$, with the streamwise location indicated on the vertical axis, for the two-dimensional case at $\alpha = 5°$. A buffer was applied to damp trailing-edge noise, ramping from zero to full effectiveness over the range $0.65 < x < 1$. The solid lines have been multiplied by $2.5 \times 10^5$ and the dashed lines by $1.25 \times 10^7$.

The onset of the buffer is downstream of the bubble, and hence any region of absolute instability present within the bubble should be unaffected, whilst upstream-travelling waves originating at the trailing edge will be damped. Figure 20 shows the time series of $dp/dt$ taken at several streamwise locations within the upper surface boundary layer. The initial response to the perturbation is the same; i.e. a downstream convecting wavepacket was observed. Upon reaching the buffer onset the wavepacket decays, and only minimal evidence of upstream-travelling acoustic waves is observed. The acoustic-feedback loop is prohibited from developing, and no disturbance growth is observed at any other location within the simulation. This appears to validate the linear stability analysis performed in §5.1; i.e. no region of absolute instability is present within the separation bubble, even when a non-parallel base flow is taken into account.

### 5.2.2. *Frequency reduction*

The frequency content of the first wavepacket observed; i.e. that produced by the initial perturbation was found to differ from that of wavepackets observed after one or more feedback-loop cycles. At $x = 0.4$, the initial wavepacket is observed to possess $f \approx 10.8$ ($\omega \approx 67.9$, figure 21a). This agrees reasonably well with linear stability analysis, which predicts that the instability wave with the maximum $N$-factor will be at $f \approx 9.6$. After three feedback-loop cycles however, the wavepacket at $x = 0.4$ is observed to reduce to $f \approx 4.0$ (figure 21b). A similar drop in frequency is observed at $x = 0.95$; the initial wavepacket possesses $f \approx 6.9$ (figure 22a), but after three feedback-loop cycles the wavepacket has $f \approx 4.0$ (figure 22b). It appears that the most unstable frequency of the acoustic-feedback loop is lower than that of the most convectively amplified instability wave over the upper aerofoil surface. This may
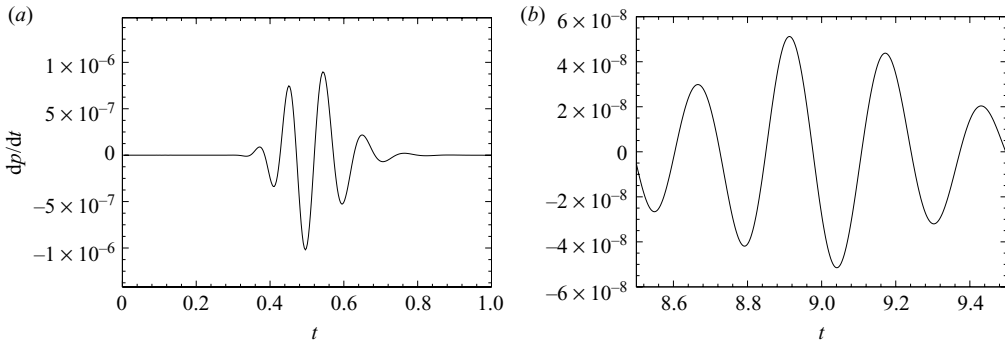
FIGURE 21. Time-dependent $dp/dt$ taken at $x = 0.4$ for the two-dimensional case at $\alpha = 5°$, showing (*a*) the initial response to the perturbation introduced at $t = 0$ and (*b*) the response after several feedback-loop cycles.
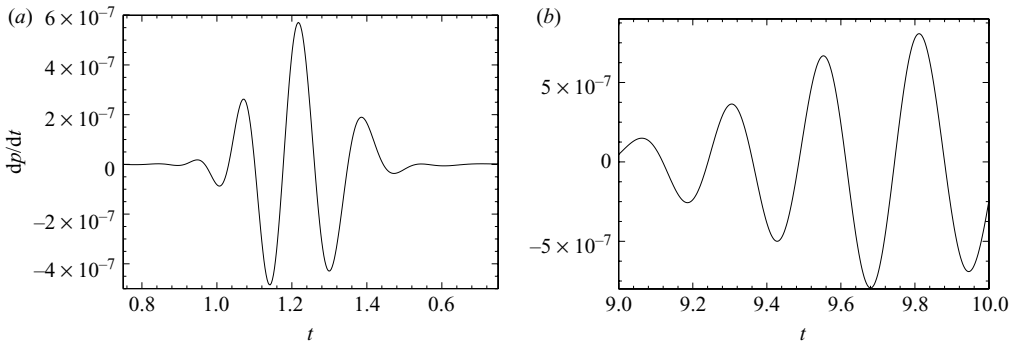


FIGURE 22. Time-dependent $dp/dt$ taken at $x = 0.95$ for the two-dimensional case at $\alpha = 5°$, showing (*a*) the initial response to the perturbation introduced at $t = 0$ and (*b*) the response after four feedback loop cycles.

explain the apparent decay in the amplitude of pressure fluctuations between the first and second wavepackets (figure 17*b*). A significant portion of the energy of the first wavepacket will be contained within frequencies which are not amplified efficiently by the feedback loop. Energy contained within these frequencies, and hence the total energy of the wavepacket, will decay initially, before the frequencies most efficiently amplified by the feedback loop grow sufficiently to recoup the energy loss.

### 5.2.3. *Relation to the developed flows*

Given that an acoustic-feedback instability has been observed in both the two- and three-dimensional time-averaged flows around an NACA-0012 aerofoil, the question must be asked as to what the implications are for the time-dependent flow.

Within the laminar region ($0 < x < 0.5$) the time-dependent flow is essentially steady, and hence the linear stability analysis is valid. The method will also accurately capture the propagation of small-amplitude (linear) acoustic waves. However, the aft section of the upper surface boundary layer ($0.5 < x < 1$) is subject to either periodic vortex shedding or the presence of a turbulent boundary layer in the unsteady two- and three-dimensional cases respectively. This violates the assumption of steady flow, and hence behaviour in this region must be considered more carefully. Gaster, Kit & Wygnanski (1985) found linear stability analysis of mean flow profiles to yield
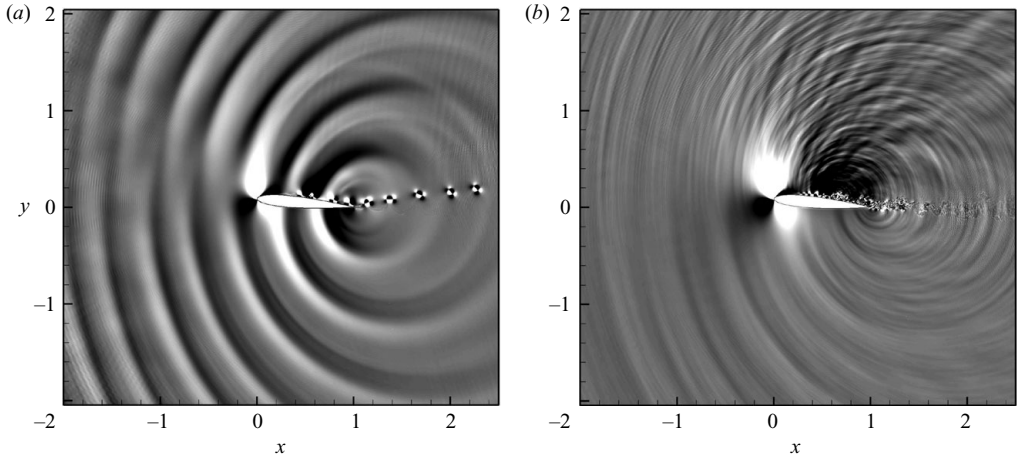
FIGURE 23. Isocontours of $\nabla \cdot U$ over the range $\pm 0.1$ for (a) two-dimensional and (b) three-dimensional simulations at $Re_c = 5 \times 10^4$, $M = 0.4$.

accurate amplitude and phase distributions for a turbulent mixing layer, although the overall amplification rates were less accurate. Barkley (2006) determined that for the case of flow around a bluff body, considering the mean flow yields a marginally stable solution, however, the frequency of global unsteadiness could be predicted comparatively accurately. This contrasts with the analysis of the (symmetrized) base flow, which was found to be unstable, and frequency predictions did not match the developed flow. Performing linear stability analysis of the time-averaged unsteady flow is felt to be useful, as long as the implications are considered. In particular, accuracy of disturbance amplification predicted within the unsteady/turbulent region cannot be guaranteed (Gaster *et al.* 1985); however the frequency content of instabilities in this region is likely to be representative of unstable modes in the developed flow (Barkley 2006).

### 5.2.4. *Frequency selection*

If the upstream-travelling acoustic waves in the fully developed flows are sufficiently large in amplitude such that receptivity and convective amplification within the separated shear layer results in nonlinear disturbance amplitudes, it is likely that the resulting disturbances (either vortical structures in two dimensions or turbulence in three dimensions) will decay only weakly before convecting over the trailing edge. These disturbances will then generate further acoustic waves capable of generating nonlinear disturbances within the separation bubble. Hence it appears possible that for the developed flows the acoustic-feedback loop may act as a frequency selection mechanism, either for the vortex shedding observed in two dimensions or for tonal behaviour in three-dimensional flow.

The two-dimensional simulation exhibits vortex shedding from the separated shear layer on the upper surface boundary layer. When the vortices convect over the aerofoil trailing edge, pressure waves are generated which convect upstream (figure 23a). A tonal acoustic response is therefore observed, even though the flow parameters are assumed in other studies to yield no tones (Lowson, Fiddes & Nash 1994). The vortex shedding occurs at frequency $f = 3.37$, which is significantly lower than the frequency of the most convectively amplified instability waves, i.e. $f \approx 8.49$. Conversely, the preferred frequency of the acoustic-feedback loop for the time-averaged

two-dimensional flow field is $f \approx 4$. These results are consistent with the hypothesis that the acoustic-feedback instability may act as a frequency selection mechanism for low-frequency vortex shedding.

Implications for the time-dependent three-dimensional simulation are more complex. Statistical data were captured for a period of 7.7 non-dimensional time units for the three-dimensional simulation, which yields good quality ensemble-averaged statistics but is insufficient for performing analysis of low-frequency fluctuations. It is therefore not possible to determine whether there is any low-frequency tonal component to either the turbulent behaviour or the fluctuating aerodynamic forces acting on the aerofoil. The possibility that a leading-edge/trailing-edge feedback loop as observed in §5.2 could lead to a tonal response in the turbulent flow cannot however be discounted. In particular, at higher Reynolds numbers the feedback loop may potentially be responsible for the generation of discrete tones of sound radiation in a similar fashion as the behaviour observed by McAlpine *et al.* (1999), although their mechanism was limited to separated flow in the trailing-edge region.

It is clearly of interest as to whether acoustic radiation observed in the developed flows is able to generate, after convective amplification, nonlinear disturbances within the separated shear layer. Furthermore, since the preferred frequency of the feedback loop is different from that of the most convectively amplified instability wave, this raises the question as to whether the receptivity process plays a role in frequency selection of the feedback loop. In order to fully describe the acoustic-feedback loop, the receptivity process will be investigated in the next section.

## 6. Receptivity of the aerofoil flow to free-stream acoustic disturbances

In this section a method for quantifying the efficiency of the receptivity process via DNS is outlined, and the receptivity process is investigated in terms of its dependency on incident acoustic wave angle and frequency.

### 6.1. *Problem definition*

A receptivity coefficient may be formed in order to quantify the efficiency of the receptivity process and is typically defined in one of two ways. The first, denoted $K_{LE}$, is to compute the ratio of hydrodynamic-to-acoustic pressure fluctuation amplitudes at $x_0 = O(a/f)$, where $a$ and $f$ are the velocity and frequency of the free-stream disturbance respectively and $x_0$ represents the region of validity for the unsteady boundary layer equations. At this streamwise location hydrodynamic pressure fluctuations will be associated with the decaying disturbance of the Lam–Rott type, and the receptivity coefficient is typically $K_{LE} = O(1)$ (e.g. see Hammerton & Kerschen 1996; Erturk & Corke 2001). The second, denoted $K_I$, is to compute the ratio of hydrodynamic-to-acoustic pressure fluctuation amplitudes at the convective instability branch point. Hydrodynamic pressure fluctuations at this location will be associated with the disturbances of the Orr–Sommerfeld type, and the receptivity coefficient will be $K_I = O(10^{-2})$–$O(10^{-1})$ (e.g. see Wanderley & Corke 2001). The problem with using the receptivity coefficient $K_I$ is that the hydrodynamic behaviour between receptivity and the instability branch point is not accounted for. This means that the receptivity coefficient will be influenced by the stability properties of the boundary layer in this region and the decay incurred during the Lam–Rott wavelength-shortening process. Conversely, the problem with using the coefficient $K_{LE}$ is that in practice it is difficult to ascertain a receptivity 'point', and it is often difficult to measure hydrodynamic disturbance amplitudes at $x = O(a/f)$ experimentally.
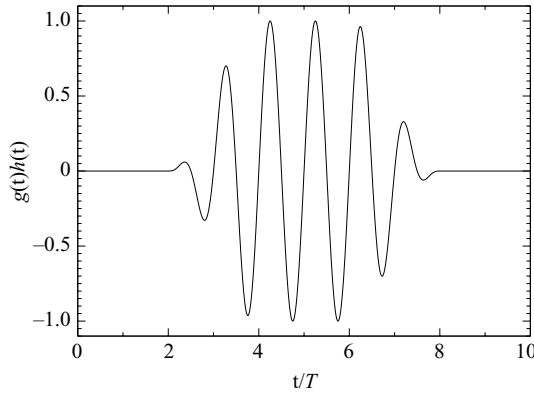
FIGURE 24. Example of the temporal variation of acoustic forcing function $g(t)h(t)$.

### 6.2. *Methodology*

In order to compute receptivity coefficients a DNS is conducted. The initial condition is the time-averaged flow of interest, in this case the three-dimensional flow around the NACA-0012 aerofoil at $\alpha = 5°$ (§ 3). Forcing terms are employed to maintain the initial condition (§ 2.3), and a forcing term $A$ (§ 2.1.2) is added to the continuity equation in order to generate acoustic waves that will strike the aerofoil. In order to differentiate between the incoming acoustic waves and any subsequent hydrodynamic response when post-processing, the acoustic forcing is employed for a finite period of time only. The forcing term, $A$, that is added to the right-hand side of the mass conservation equation (§ 2.1.2) is defined as

$$A = \phi(x, y)g(t)h(t). \tag{6.1}$$

The function $\phi(x, y)$ specifies the size and shape of the forcing region and, for a specified forcing location $(x_0, y_0)$ and radius $R$, is defined as

$$\left.\begin{array}{ll} r < R : & \phi(x, y) = \dfrac{1}{2}\left[1 + \cos\left(\dfrac{\pi r}{R}\right)\right], \\[2mm] r > R : & \phi(x, y) = 0, \end{array}\right\} \tag{6.2}$$

where $r^2 = (x_0 - x)^2 + (y_0 - y)^2$. Functions $g(t)$ and $h(t)$ control the frequency and envelope of the acoustic pulse respectively. Function $g(t)$ is a simple sine wave,

$$g(t) = \sin(2\pi f t), \tag{6.3}$$

where $f$ is the specified disturbance frequency. Function $h(t)$ windows the acoustic pulse, smoothly ramping from zero amplitude to a maximum and then back to zero again, over a finite number of disturbance periods. Function $h(t)$ is defined as

$$\left.\begin{array}{ll} 0 < t < \dfrac{n_r}{f} : & h(t) = \dfrac{1}{2}\left[1 - \cos\left(\dfrac{f}{n_r}\pi t\right)\right], \\[3mm] \dfrac{n_r}{f} < t < \dfrac{n_t}{f} - \dfrac{n_r}{f} : & h(t) = 1, \\[3mm] \dfrac{n_t}{f} - \dfrac{n_r}{f} < t < \dfrac{n_t}{f} : & h(t) = \dfrac{1}{2}\left[1 - \cos\left(\left[\dfrac{n_t}{n_r} - \dfrac{f t}{n_r}\right], \pi\right)\right], \end{array}\right\} \tag{6.4}$$

where $n_t$ is the total number of disturbance periods and $n_r$ is the number of disturbance periods over which the function $h(t)$ increases from 0 to 1. Figure 24
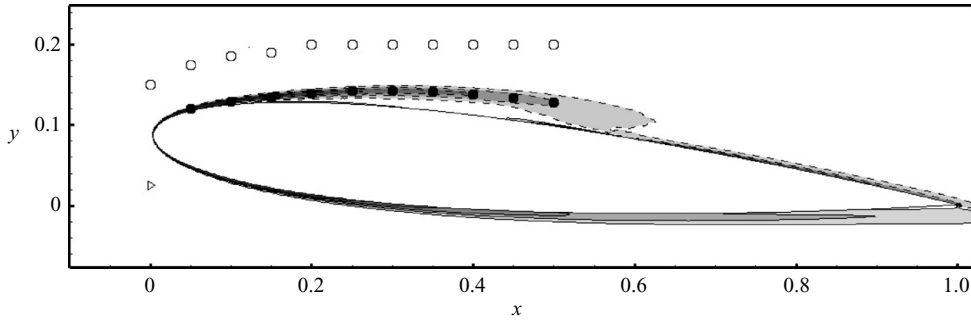
FIGURE 25. Pressure measurement locations for the receptivity study. The filled circles represent the location of maximum vorticity within the aerofoil boundary layer, whilst the open circles represent locations outside the aerofoil boundary layer where acoustic pressure fluctuations will be dominant. The triangle indicates a reference location for measuring acoustic pressure below the aerofoil.

displays $g(t)h(t)$ as computed for $f = 1$, $n_r = 2$ and $n_t = 6$, clearly illustrating the resultant wavepacket and envelope.

When the aerofoil is subject to acoustic excitation, hydrodynamic instability waves are expected to be generated within the upper surface boundary layer. The incoming acoustic pressure fluctuations and resultant boundary layer instabilities are monitored by recording the pressure signal at many 'probe' locations, as illustrated in figure 25. Ten probes are placed within the boundary layer, spaced in an equidistant manner over the range $0.05 \leqslant x \leqslant 0.5$. The $y$-location is specified as the point of maximum mean vorticity magnitude within the aerofoil boundary layer, where the maximum $p'$ associated with hydrodynamic instability waves is expected. A further 11 probes are placed in the free stream, just outside the boundary layer, spaced in an equidistant manner over the range $0 \leqslant x \leqslant 0.5$. The $y$-location is to some degree arbitrary but is chosen to be near enough to the boundary layer to give a good representation of acoustic wave amplitude near the boundary layer edge whilst ensuring spanwise vorticity is small in value ($\omega_z < 1 \times 10^{-3}$).

### 6.3. *Receptivity to acoustic pulse at* $f = 8.49$

To study the receptivity process the time-averaged flow field of the three-dimensional flow around an NACA-0012 aerofoil at $\alpha = 5°$ was subjected to an incident acoustic wavepacket, generated in the manner given in §6.2. The frequency of the acoustic wavepacket was specified as $f = 8.49$, with $n_r = 2$ and $n_t = 6$. The forcing location was specified as $(x, y) = (2.142, 1.142)$, a location downstream of and above the aerofoil.

Acoustic waves are radiated from the forcing location in all directions, propagating at the local sound speed and hence with non-uniform directivity about the forcing location, because of the non-zero Mach number of the flow (figure 26$a$). It should be noted that although the method of forcing represents a monopole source, because of the non-zero velocity of the base flow the acoustic wavefront is not uniform, and the acoustic perturbation exhibits two regions of decreased amplitude. When the acoustic wavepacket reaches the aerofoil the receptivity process ensues, and a downstream-travelling hydrodynamic wavepacket is generated, as observed in figure 26($b$).

Figure 27($a$) shows $x/t$ plots of pressure disturbances in the region $0.05 < x < 0.5$ just outside the aerofoil boundary layer where the acoustic response is dominant. The initial acoustic wavepacket can be observed to propagate upstream, as indicated by the negative slope of the wavepacket trajectory, and does not appear to vary in amplitude
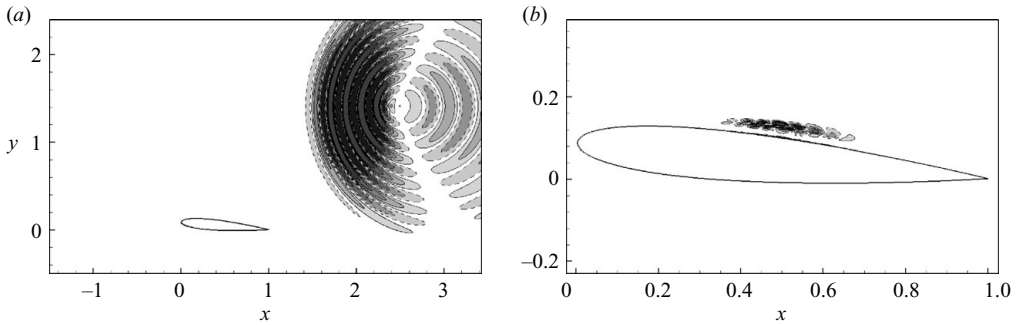
FIGURE 26. (*a*) Isocontours of $\nabla U'$ taken at $t = 0.7$, using 20 levels over the range $\pm 1.5 \times 10^{-7}$, and (*b*) isocontours of $\omega'_z$ taken at $t = 2.8$, using 10 levels over the range $\pm 2.5 \times 10^{-3}$, with acoustic wavepacket excited at $f = 8.49$, $(x, y) = (2.142, 1.142)$. The negative contours are represented with the dashed lines.
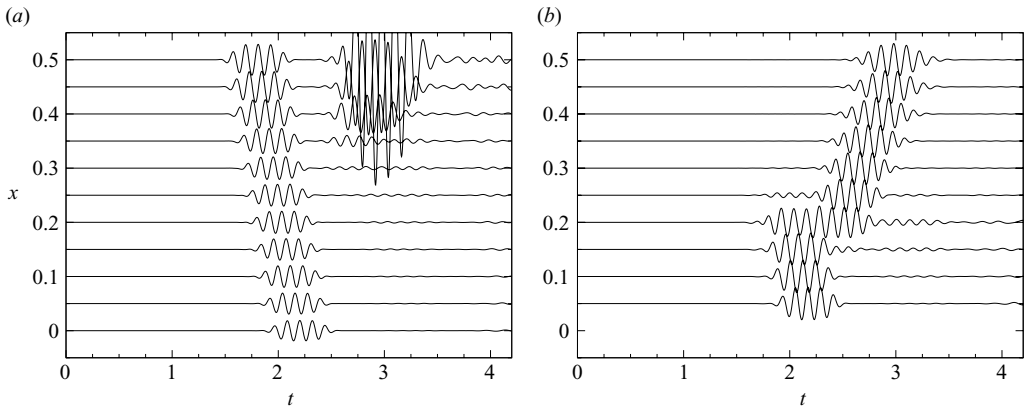


FIGURE 27. Time-dependent pressure, with the streamwise location indicated on the vertical axis, plotted (*a*) outside the boundary layer where the acoustic response is dominant and (*b*) within the boundary layer where the hydrodynamic response is dominant. For the right-hand-side image, the pressure signal at each $x$-location has been normalized by the maximum pressure observed at that $x$-location.

to any significant degree as it does so. When the acoustic wavepacket reaches the leading edge a downstream-travelling hydrodynamic wavepacket is generated. The hydrodynamic response can be observed in figure 27(*a*); however it is more clearly illustrated by plotting pressure fluctuations within the boundary layer itself. Convective instability growth rates are large at this frequency; hence the fluctuations for $x < 0.4$ are hard to discern when plotting pressure data scaled with the largest amplitude fluctuations present over the entire aerofoil. An alternative method is to normalize the pressure series at each $x$-location by the maximum pressure fluctuation observed at the $x$-location in question. This means that the amplitude of fluctuations cannot be compared between $x$-locations; however the wavepacket trajectory is now visible. Pressure fluctuations within the aerofoil boundary layer are plotted in this manner in figure 27(*b*). The downstream-travelling hydrodynamic wavepacket can readily be distinguished in the region $0.25 < x < 0.5$, where it is the largest amplitude fluctuation present. Upstream of $x = 0.2$ the dominant pressure fluctuations take the form of the upstream-travelling acoustic wavepacket. In this region any boundary
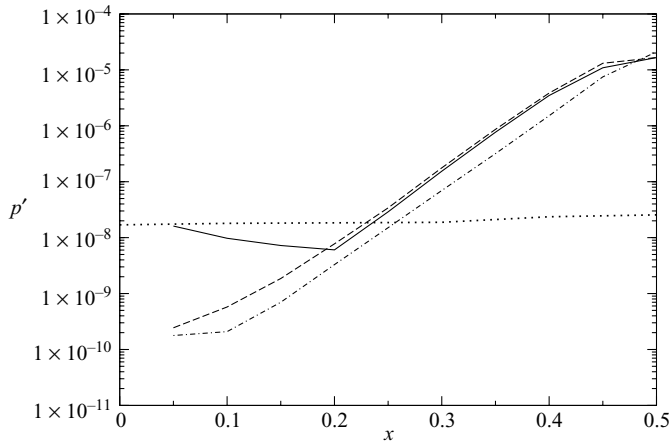
FIGURE 28. Amplitude of pressure fluctuations as a function of $x$, recorded at locations within the aerofoil boundary layer (—) and outside the aerofoil boundary layer ($\cdots$), and the equivalent instability growth curve as computed via DNS (– –) and LST (–·).

layer disturbance present must be small in comparison with the pressure fluctuations resulting because of the passage of the acoustic wavepacket. At $x = 0.2$ the amplitudes of hydrodynamic and acoustic pressure fluctuations appears to be approximately the same.

Although it is possible to determine an approximate $x(t)$ for both the acoustic and hydrodynamic wavepackets from figure 27, it is difficult to determine at which 'point' the receptivity process takes place. Acoustic and hydrodynamic pressure fluctuations appear to be similar in amplitude at $x = 0.2$; however this does not imply that $x = 0.2$ is a location of receptivity; the wavepacket trajectories in figure 27 suggest that the wavepackets intersect somewhere in the region $0 < x < 0.05$. The receptivity coefficient $K_{LE}$ would be evaluated at $x_0 = O(a/2\pi f)$ which, assuming an acoustic wave velocity of $a = 1.5$, corresponds to $x \approx 0.03$. However, in the current study it is not possible to distinguish pressure fluctuations associated with the hydrodynamic response from those associated with the acoustic wavepacket in this region; so $K_{LE}$ cannot be computed. Downstream of $x = 0.2$ the behaviour of the hydrodynamic wavepacket corresponds to that of convective instability growth. It is therefore possible to extrapolate the wavepacket amplitude upstream to estimate the disturbance amplitude at, for example, the neutral point for convective instability. Thus it is possible to compute $K_I$.

Pressure disturbance amplitudes as a function of $x$ are plotted in figure 28. It can be seen that the amplitude of the acoustic wave decreases only slightly with upstream propagation. The amplitude of pressure fluctuations in the boundary layer varies more dramatically. In the region $0.05 < x < 0.2$ the amplitude of pressure fluctuations within the boundary layer decreases with increasing $x$. Cross-referencing with figure 27 shows that pressure fluctuations observed in this region correspond to the upstream-propagating acoustic wave. The fact that the pressure fluctuations decrease with increasing $x$ suggests that the acoustic wave is able to penetrate the boundary layer more effectively as the leading edge is approached. Similar qualitative behaviour was predicted by Jacobs & Durbin (1998) who, in a study of the continuous Orr–Sommerfeld spectrum, determined that free-stream disturbances will penetrate a boundary layer to a greater depth as the Reynolds number based on boundary
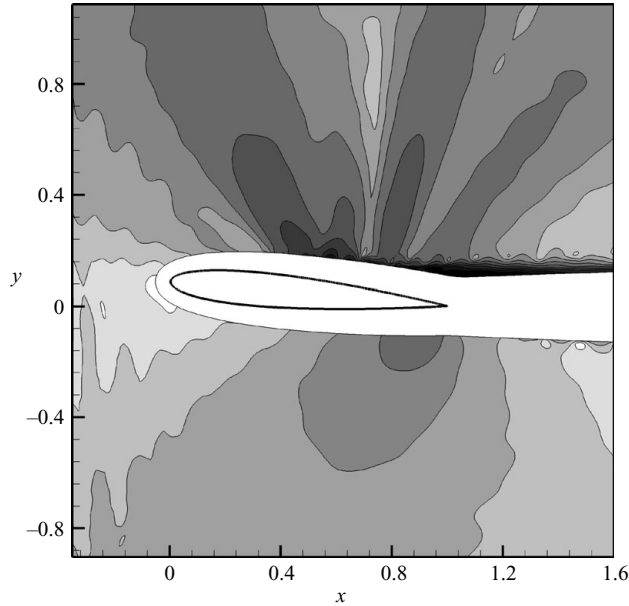
FIGURE 29. Modulus of pressure at $f = 8.49$, taken at the mid-span of the three-dimensional simulation, showing 10 levels exponentially distributed over the range $1 \times 10^{-5} - 1 \times 10^{-3}$.

layer thickness (and disturbance frequency) is decreased. In the region $0.2 < x < 0.5$ the pressure fluctuations observed in the boundary layer are generated by a hydrodynamic wavepacket convecting downstream (see figure 27). Given that $f = 8.49$, we can use the data from this region to extrapolate the amplitude envelope of the hydrodynamic instability upstream to a location of our choice. Convective instability growth curves generated via both classical LST and DNS (see §4.1) are plotted in figure 28 alongside the results from the receptivity study. Both sets of data have been scaled such that the amplitude at $x = 0.5$ matches that observed in the receptivity study. It can be seen that the curve generated via LST does not match the data very closely in the region $0.2 < x < 0.5$, primarily because of discrepancies in the region $0.45 < x < 0.5$, whereas the growth rate obtained via DNS matches well. If we consider the point $x = 0.05$, corresponding to the neutral point for convective instability growth, we can now estimate an instability wave amplitude at this location, as $p' = 2.4 \times 10^{-10}$. Given an acoustic wave amplitude of $p' = 1.7 \times 10^{-8}$ at the same location, the resultant receptivity coefficient is $K_I = 1.4 \times 10^{-2}$, a similar order of magnitude as that observed in other studies (e.g Erturk & Corke 2001). Furthermore, the ratio of the maximum hydrodynamic disturbance amplitude (at $x = 0.5$) to the acoustic wave amplitude (at $x = 0.05$) is $1 \times 10^3$. This means that acoustic excitation at $f = 8.49$ with amplitude $1 \times 10^{-5}$ would be sufficient to generate hydrodynamic instabilities at nonlinear (i.e. $O(1 \times 10^{-2})$) amplitudes. A spectral analysis of the free-stream pressure at the aerofoil mid-span of the original three-dimensional simulation illustrates that at $x = 0.05$ pressure fluctuations at $f = 8.49$ are $2.5 \times 10^{-5}$ in amplitude (figure 29). This suggests that the aerofoil self-noise present in the three-dimensional simulation is potentially large enough in amplitude to sustain the transition process. Self-sustaining transition to turbulence was indeed observed in the three-dimensional simulation; however it was attributed to a three-dimensional absolute instability of the naturally occurring

| Angle about $(x, y) = (0.5, 0)$ | $x$ | $y$ |
|---|---|---|
| 0° | 3 | 0 |
| 36.5° | 2.414 | 1.414 |
| 90° | 0.5 | 2 |
| 143.5° | −1.414 | 1.414 |
| 180° | −2 | 0 |
| 216.5° | −1.414 | −1.414 |
| 270° | 0.5 | −2 |
| 323.5° | 2.414 | −1.414 |

TABLE 2. Acoustic source coordinates used for the study of receptivity behaviour with varying source location.

vortex shedding, a mechanism which is more rapid than the present feedback loop (Jones *et al.* 2008).

For the three-dimensional simulation at $x = 0.05$, the amplitude of acoustic pressure fluctuations at $f = 3.37$ (the vortex-shedding frequency) is an order of magnitude greater than at $f = 8.49$. In the two-dimensional simulation the acoustic pressure fluctuations at this frequency are even greater in amplitude, because of the narrowband frequency content of the flow. It is apparent that where vortex shedding occurs, the resulting trailing-edge noise will excite the separated shear layer via the receptivity process, ultimately generating disturbances at nonlinear amplitudes within the separated shear layer. In conjunction with the observations regarding frequency content in §5.2.4, these results support the hypothesis that the acoustic-feedback mechanism plays a role in frequency selection for the naturally occurring vortex shedding.

### 6.4. *Dependency of the receptivity process on source location*

Having defined a technique for quantifying the receptivity process, the dependency of receptivity efficiency upon various parameters can now be determined. First, the dependency of receptivity efficiency upon the direction of the initial acoustic disturbance is investigated. This is performed for the fixed frequency $f = 8.49$. Simulations are performed in the same manner as in §6.3 whilst varying the location of the acoustic source. Eight simulations are performed in total, for which the acoustic source coordinates are given in table 2 and plotted in figure 30.

Receptivity coefficients computed in the same manner as in §6.3 are plotted versus the angle about $(x, y) = (0.5, 0)$ in figure 31. It is apparent that the receptivity coefficient is lowest when the acoustic source is directly downstream of the aerofoil. More striking is the fact that the receptivity coefficient is significantly larger when the acoustic source is below the aerofoil than when the source is above the aerofoil. This result is surprising, since receptivity and instability growth are observed for the upper surface boundary layer. A possible explanation would be that if the stagnation point, which is located slightly below the aerofoil chord line (figure 10), were the critical location with regard to receptivity, then the acoustic amplitudes experienced at the stagnation point would be greater than those suggested by the probe measurements presented here. Defining the receptivity coefficient based on the acoustic pressure as recorded below the aerofoil, at $x = 0.05$, results in a different variation of receptivity with source location that is comparatively flatter and more symmetric (figure 31). Erturk & Corke (2001) computed the receptivity coefficient $K_{LE}$ as a function of acoustic wave incidence for a parabolic body, by solving incompressible linear
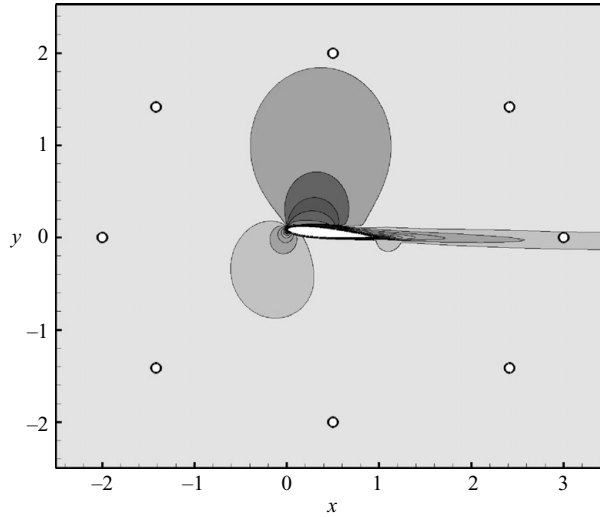
FIGURE 30. Locations at which the acoustic source is applied for the study of receptivity behaviour with varying source location.
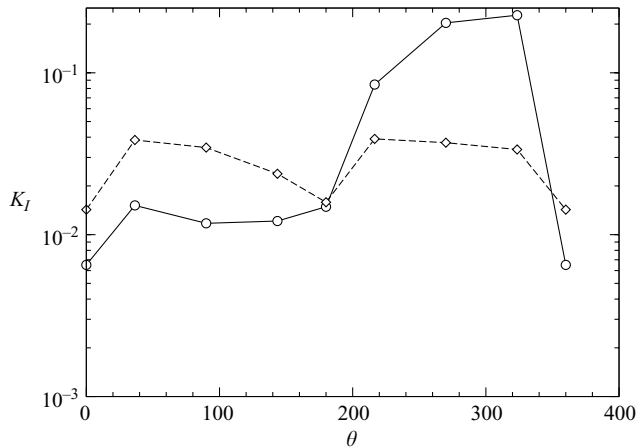


FIGURE 31. Variation of the receptivity coefficient with the angle about $(x, y) = (0.5, 0)$, with the positive $x$-axis specified as $\theta = 0°$, and the receptivity coefficient defined as measuring acoustic pressure above the aerofoil ($\bigcirc$—$\bigcirc$) and below the aerofoil ($\diamond - -\diamond$).

perturbation equations in conjunction with a steady base flow. Erturk & Corke (2001) observed maximum values of $K_{LE}$ for $\theta = \pm 90°$, and minimum values for $\theta \approx 0°$, appearing qualitatively similar to the data plotted in figure 31 normalized by lower surface pressure.

### 6.5. Dependency of the receptivity process on frequency

The frequency dependency of the receptivity process is investigated by following the same method as in § 6.3, keeping the source location constant whilst varying the disturbance frequency. The lowest frequency for which results are presented is $f = 6.1$. Below $f = 6.1$ the increased temporal length of the acoustic wavepacket means that the acoustic and hydrodynamic wavepackets are inseparable. The source location is specified as $(x, y) = (2, 0.4)$. Acoustic waves originating from this location
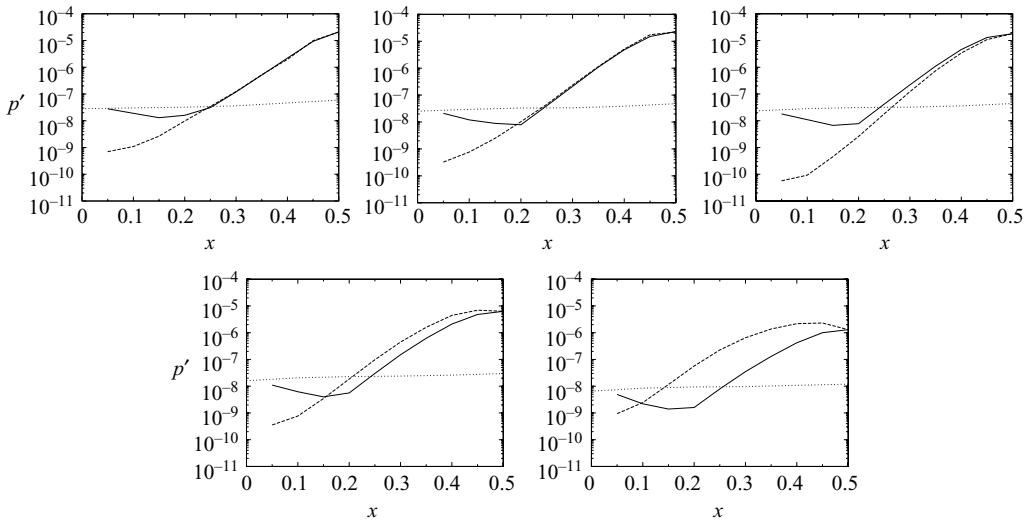
FIGURE 32. Amplitude of pressure fluctuations as a function of $x$, recorded at locations within the aerofoil boundary layer (—), outside the aerofoil boundary layer ($\cdots$) and the equivalent instability growth curve as computed via DNS (– –). From left to right, the top row shows $f = 6.1$, $f = 8.49$ and $f = 9.15$, and the bottom row shows $f = 11.2$ and $f = 14.25$.

will propagate upstream, in a fashion similar to acoustic waves originating at the aerofoil trailing edge.

### 6.5.1. *Results*

The variation of pressure fluctuation amplitude with $x$ both within and immediately outside the boundary layer is plotted in figure 32, alongside equivalent convective disturbance growth curves, for all frequencies investigated. It is apparent that whilst the amplitudes of fluctuations in the boundary closely layer match $e^N$ curves computed via DNS for $f = 6.1$ and $f = 8.49$, they do not match very well for $f = 11.2$ and above. Analysing the frequency content of the hydrodynamic instability waves explains why this is the case.

The frequency of the hydrodynamic wavepacket ($f_{hy}$) is plotted against that of the acoustic ($f_{ac}$) wavepacket in figure 33. It can be seen that for high frequencies there is a noticeable discrepancy between the two quantities. For example, when the aerofoil is subject to an acoustic pulse at $f = 14.25$ the resultant hydrodynamic wavepacket occurs at $f \approx 9.8$. When the results of each receptivity study are plotted alongside $e^N$ curves for frequencies matching the actual hydrodynamic instability wave, as opposed to those matching the expected hydrodynamic instability wave, the variation of amplitude with $x$ is matched much more closely (figure 34).

To understand why an acoustic wavepacket with a dominant frequency generates a boundary layer instability wave with a significantly different frequency we must return to the wavepacket structure. The requirement that the acoustic excitation is finite in time necessitates the use of the ramping function $h(t)$ (§ 6.2). The use of the ramping function means that the acoustic wavepacket will contain energy not only at frequency $f$, as specified by the function $g(t)$, but also at other frequencies introduced by the window envelope $h(t)$. Plotting power spectra of the excitation wavepacket illustrates the energy content (figure 35). It can be seen that energy is contained over a small range of frequencies near the input frequency. The $N$-factor across the separation
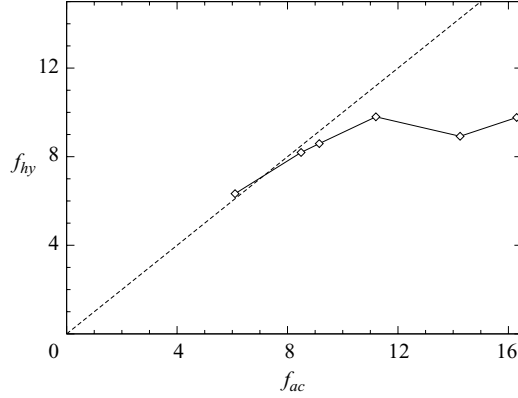
FIGURE 33. Frequency of the acoustic pulse versus frequency of the induced
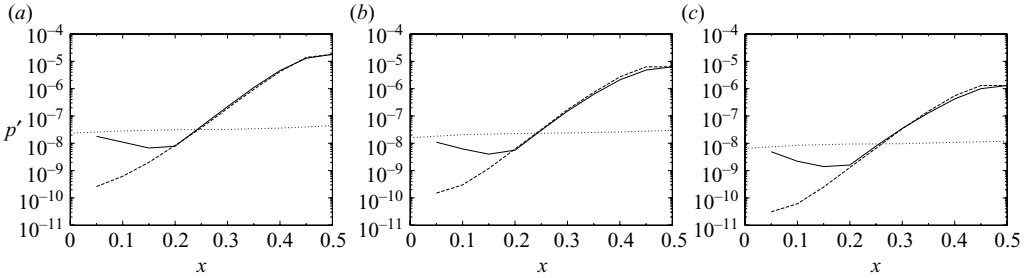hydrodynamic wavepacket.



FIGURE 34. Amplitude of pressure fluctuations as a function of $x$, recorded at locations within
the aerofoil boundary layer (—), outside the aerofoil boundary layer ($\cdots$) and an instability
growth curve as computed via DNS (– –). The frequency of the instability growth prediction
($f_i$) is different from that of the acoustic wave input ($f_{ac}$): ($a$) shows acoustic frequency
$f_{ac} = 9.15$ plotted with instability growth for $f_i = 8.49$; ($b$) shows $f_{ac} = 11.2$ plotted with
$f_i = 9.8$; ($c$) shows acoustic frequency $f_{ac} = 14.25$ plotted with $f_i = 9.8$.

bubble at $f = 14.85$ is $N \approx 10$, whereas for $f = 8.49$ $N \approx 13$. Assuming disturbances
of the same initial amplitude originating at $x = 0.05$, this means that disturbances at
$f = 8.49$ will be amplified by a factor approximately 55 times greater than those at
$f = 14.85$. Hence it is likely that for a wavepacket formed in the manner specified in
§6.2, subsequent to receptivity the frequency selection of the convective disturbance
amplification process modifies the disturbance wavepacket to such an extent that the
specified frequency of interest, $f$, is no longer the dominant frequency.

Given that the frequency dependency of the convective disturbance growth alters
the frequency content of the disturbance wavepacket, interpretation of results must be
considered carefully. Where acoustic excitation is applied at a frequency higher than
that of the most convectively amplified instability wave, i.e. $f_{ac} > 8.49$, the resultant
hydrodynamic wavepacket is observed to possess frequency $f_{hy} < f_{ac}$. Whatever the
amplitude of the hydrodynamic instability wave at $x = 0.5$, it can be said that the
instability wave will contain less energy at $f_{ac}$ than at $f_{hy}$, since $f_{ac}$ is no longer
the dominant frequency. If we were to extrapolate the disturbance amplitude back to
$x = 0.05$ using an $e^n$ curve formed for $f_{ac}$ but using the amplitude of the disturbance at
$x = 0.5$ where the dominant frequency is $f_{hy}$, we would obtain a maximum disturbance
amplitude at $x = 0.05$. It is probable that the disturbance amplitude at $f_{ac}$ will be
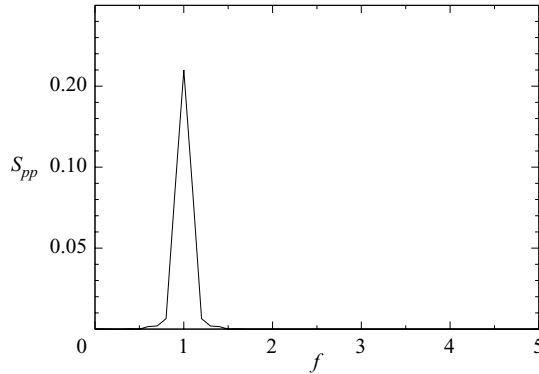
FIGURE 35. Power spectra of the acoustic forcing function $g(t)h(t)$ plotted versus non-dimensional frequency.
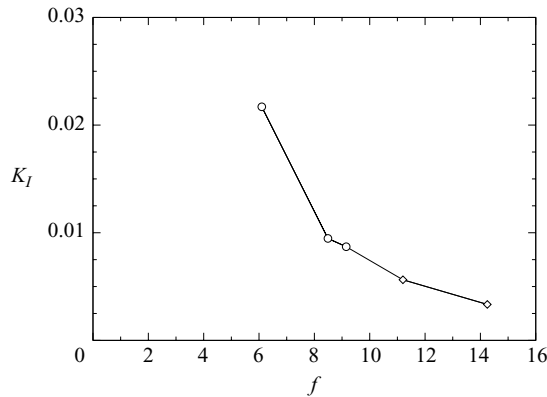


FIGURE 36. Variation of the receptivity coefficient with frequency: ○ indicates actual values; ◇ indicates upper limits.

significantly less than that computed, but it cannot be any greater. This means that although we cannot accurately compute $K_I$, we can compute an upper limit for $K_I$.

The upper limit for $K_I$ is plotted for frequencies $f \geqslant 11.2$ alongside actual values for $K_I$ for $f < 8, 49$ in figure 36. It is apparent that for $f = 9.15$ and below, the receptivity coefficients are significantly larger than even the maximum possible values for $f = 11.2$ and above, and hence the receptivity coefficient decreases with increasing frequency. Two possible reasons for this trend are hypothesized. Firstly, the study of Jacobs & Durbin (1998) suggests that free-stream disturbances will penetrate boundary layers more effectively at low frequency. Secondly, it is known that acoustic receptivity requires a streamwise variation in boundary layer structure (Goldstein 1983). A streamwise variation in boundary layer structure will appear 'sharper' to a low-frequency acoustic wave than for a high-frequency acoustic wave, since the acoustic wavelength will be greater. The analogy here is with the scattering of acoustic waves over a finite-radius leading or trailing edge. The fact that the receptivity process appears to be increasingly efficient at low frequencies suggests that the receptivity process plays an important role in selecting the comparatively low preferred frequency ($f \approx 4$) of the acoustic-feedback loop observed in §5.2.2.

## 7. Conclusions

Linear stability analysis of the time-averaged two- and three-dimensional flows around an NACA-0012 aerofoil at $\alpha = 5°$ has been performed. The frequency of the most amplified instability wave is significantly higher than that of the vortex-shedding behaviour observed in two dimensions. This appears to discount viscous or inviscid convective instability growth as the primary frequency selection mechanism for the vortex shedding. For both cases classical linear stability analysis accurately predicts the frequency of the most amplified wave; however integrating disturbances along the aerofoil surface results in disturbance amplitudes that are consistently larger than those obtained by DNS.

No evidence of local absolute instability was observed when a cusp-map analysis was performed. This was confirmed by performing two-dimensional linear stability analysis via forced Navier–Stokes simulations. Forced Navier–Stokes simulations did however determine that both time-averaged flow fields are unstable because of an acoustic-feedback instability, in which instability waves convecting over the trailing edge of the aerofoil generate acoustic waves that propagate upstream to some location of receptivity and generate further instability waves within the boundary layer. As the cycle repeats, the amplitude of both hydrodynamic instabilities and acoustic waves increases. The resultant behaviour may be defined as globally unstable, although no local absolute instability is present. The preferred frequency of the acoustic-feedback loop is significantly lower than that of the most convectively amplified instability wave and is comparable to that of the vortex shedding observed in two dimensions. It is therefore suggested that the acoustic-feedback loop may play a role in frequency selection for the vortex shedding that occurs naturally.

The receptivity process, which is necessary for the acoustic-feedback loop to occur, has been investigated by performing forced Navier–Stokes simulations of the time-averaged flow around an aerofoil subject to an acoustic pulse. In this manner it is possible to determine the amplitude of the hydrodynamic disturbances that would result when the aerofoil is subject to an acoustic disturbance of a given amplitude. For the frequency of the most convectively amplified instability wave it was determined that an acoustic wave of amplitude $O(1.1 \times 10^{-5})$ would generate boundary layer disturbances of the amplitude $O(1 \times 10^{-2})$. This suggests that for the current case aerofoil self-noise may play a role in the transition process and confirms that the naturally occurring vortex shedding will generate nonlinear disturbances in the separated shear layer via the feedback mechanism. The dependency of the receptivity process on acoustic wave angle was investigated, and the receptivity coefficient was observed to be a minimum when the acoustic source was located either directly upstream or directly downstream of the aerofoil. The receptivity coefficient was found to decrease significantly with increasing frequency of the incident acoustic wave. It is likely that this behaviour is in part responsible for the preferred frequency of the acoustic-feedback loop being lower than that of the most convectively amplified instability wave.

## REFERENCES

ALAM, M. & SANDHAM, N. D. 2000 Direct numerical simulation of short laminar separation bubbles with turbulent reattachment. *J. Fluid Mech.* **410**, 1–28.

BARKLEY, D. 2006 Linear analysis of the cylinder wake mean flow. *Europhys. Lett.* **75** (5), 750–756.

CARPENTER, M. H., NORDSTRÖM, J. & GOTTLIEB, D. 1999 A stable and conservative interface treatment of arbitrary spatial accuracy. *J. Comput. Phys.* **148** (2), 341–365.

DENG, S., JIANG, L. & LIU, C. 2007 DNS for flow separation control around an airfoil by pulsed jets. *Comp. Fluids* **36** (6), 1040–1060.

DESQUESNES, G., TERRACOL, M. & SAGAUT, P. 2007 Numerical investigation of the tone noise mechanism over laminar airfoils. *J. Fluid Mech.* **591**, 155–182.

DRAZIN, P. G. & REED, W. H. 1981 *Hydrodynamic Stability*. Cambridge University Press.

DRELA, M. & GILES, M. B. 1987 Viscous-inviscid analysis of transonic and low Reynolds number airfoils. *AIAA J.* **25** (10), 1347–1355.

ERTURK, E. & CORKE, T. C. 2001 Boundary layer leading-edge receptivity to sound at incidence angles. *J. Fluid Mech.* **444**, 383–407.

FFOWCS WILLIAMS, J. E. & HALL, L. H. 1970 Aerodynamic sound generation by turbulent flow in the vicinity of a scattering half-plane. *J. Fluid Mech.* **40** (4), 657–670.

GASTER, M. 1963 On stability of parallel flows and the behaviour of separation bubbles. PhD thesis, University of London, London.

GASTER, M. 1968 Growth of disturbances in both space and time. *Phys. Fluids* **11**, 723–727.

GASTER, M. 1978 Series representation of the eigenvalues of the Orr–Sommerfeld equation. *J. Comput. Phys.* **29**, 147–162.

GASTER, M., KIT, E. & WYGNANSKI, I. 1985 Large-scale structures in a forced turbulent mixing layer. *J. Fluid Mech.* **150**, 23–39.

GOLDSTEIN, M. E. 1983 The evolution of Tollmien–Schlichting waves near a leading edge. *J. Fluid Mech.* **127**, 59–81.

HADDAD, O. M., ERTURK, E. & CORKE, T. C. 2005 Acoustic receptivity of the boundary layer over parabolic bodies at angles of attack. *J. Fluid Mech.* **536**, 377–400.

HAMMERTON, P. W. & KERSCHEN, E. J. 1996 Boundary-layer receptivity for a parabolic leading edge. *J. Fluid Mech.* **310**, 243–267.

HAMMOND, D. A. & REDEKOPP, L. G. 1998 Local and global instability properties of separation bubbles. *Eur. J. Mech.* B **17** (2), 145–164.

HANNEMANN, K. & OERTEL, H. 1989 Numerical simulation of the absolutely and convectively unstable wake. *J. Fluid Mech.* **199**, 55–88.

HERBERT, TH. 1997 Parabolized stability equations. *Annu. Rev. Fluid Mech.* **29**, 245–283.

HORTON, H.P. 1968 Laminar separation in two- and three-dimensional incompressible flow. PhD thesis, University of London, London.

HUERRE, P. & MONKEWITZ, P. A. 1985 Absolute and convective instabilities in free shear layers. *J. Fluid Mech.* **159**, 151–168.

HUERRE, P. & MONKEWITZ, P. A. 1990 Local and global instabilities in spatially developing flows. *Annu. Rev. Fluid Mech.* **22**, 473–537.

JACOBS, R. G. & DURBIN, P. A. 1998 Shear sheltering and the continuous spectrum of the Orr–Sommerfeld equation. *Phys. Fluids* **10**, 2006–2011.

JONES, L. E. 2007 Numerical studies of the flow around an airfoil at low Reynolds number. PhD thesis, University of Southampton, Southampton, UK .

JONES, L. E., SANDBERG, R. S. & SANDHAM, N. D 2008 Direct numerical simulations of forced and unforced separation bubbles on an airfoil at incidence. *J. Fluid Mech.* **602**, 175–207.

KACHANOV, Y. S. 1994 Physical mechanisms of laminar-boundary-layer transition. *Annu. Rev. Fluid Mech.* **26** (1), 411–482.

LAM, S. H. & ROTT, N. 1960 *Theory of Linearized Time-Dependent Boundary Layers*. Graduate School of Aeronautical Engineering, Cornell University.

LEE, C. B. & WU, J. Z. 2008 Transition in wall-bounded flows. *Appl. Mech. Rev.* **61**, 1–32.

LELE, S. K. 1992 Compact finite difference schemes with spectral-like resolution. *J. Comput. Phys.* **103**, 16–42.

LOWSON, M. V., FIDDES, S. P. & NASH, E. C. 1994 Laminar boundary layer aeroacoustic instabilities. *Paper* 94-0358. AIAA.

MARQUILLIE, M. & EHRENSTEIN, U. W. E. 2003 On the onset of nonlinear oscillations in a separating boundary-layer flow. *J. Fluid Mech.* **490**, 169–188.

MCALPINE, A., NASH, E. C. & LOWSON, M. V. 1999 On the generation of discrete frequency tones by the flow around an airfoil. *J. Sound Vib.* **222** (5), 753–779.

MORKOVIN, M. 1984 Bypass transition to turbulence and research desiderata. In *Transition in Turbines* (ed. R. Graham), *NASA Conf. Pub. 2386*, pp. 161–204.

MORKOVIN, M., RESHOTKO, E. & HERBERT, T. 1994 Transition in open flow systems – a reassessment. *Bull. Am. Phys. Soc.* **39** (9), 1882.

PAULEY, L. L., MOIN, P. & REYNOLDS, W. C. 1990 The structure of two-dimensional separation. *J. Fluid Mech.* **220**, 397–411.

RADESPIEL, J. W. & SCHOLZ, U. 2007 Numerical and experimental flow analysis of moving airfoils with laminar separation bubbles. *AIAA J.* **45** (6), 1346–1356.

ROSSITER, J. E. 1964 Wind-tunnel experiments on the flow over rectangular cavities at subsonic and transonic speeds. *Aeronaut. Res. Counc. Rep. Memo* **3838**.

SANDBERG, R. D., JONES, L. E., SANDHAM, N. D. & JOSEPH, P. F. 2009 Direct numerical simulations of tonal noise generated by laminar flow past airfoils. *J. Sound Vib.* **320**, 838–858.

SANDBERG, R. D. & SANDHAM, N. D. 2008 Direct numerical simulation of turbulent flow past a trailing-edge and the associated noise generation. *J. Fluid Mech.* **596**, 353–385.

SANDBERG, R. D., SANDHAM, N. D. & JOSEPH, P. F. 2007 Direct numerical simulations of trailing-edge noise generated by boundary-layer instabilities. *J. Sound Vib.* **304**, 677–690.

SANDHAM, N. D. 2008 Transitional separation bubbles and unsteady aspects of aerofoil stall. *Aeronaut. J.* **112** (1133), 395–404.

SANDHAM, N. D. & KLEISER, L. 1992 The late stages of transition to turbulence in channel flow. *J. Fluid Mech.* **245**, 319–347.

SANDHAM, N. D., LI, Q. & YEE, H. C. 2003 Entropy splitting for high-order numerical simulation of compressible turbulence. *J. Comput. Phys.* **178**, 307–322.

SARIC, W. S., REED, H. L. & KERSCHEN, E. J. 2002 Boundary-layer receptivity to free stream disturbances. *Annu. Rev. Fluid Mech.* **34** (1), 291–319.

SCHMID, P. J. & HENNINGSON, D. S. 2001 *Stability and transition in shear flows*. Springer.

THEOFILIS, V. 2003 Advances in global linear instability analysis of nonparallel and three-dimensional flows. *Progr. Aerosp. Sci.* **39**, 249–315.

TORRES, G. E. & MUELLER, T. J. 2001 Aerodynamic characteristics of low aspect ratio wings at low Reynolds numbers. In *Fixed and Flapping Wing Aerodynamics for Micro Air Vehicle Applications* (ed. T. J. Mueller), pp. 115–141, AIAA.

WANDERLEY, J. B. V. & CORKE, T. C. 2001 Boundary layer receptivity to free-stream sound on elliptic leading edges of flat plates. *J. Fluid Mech.* **429**, 1–21.

WHITE, F. M. 1991 *Viscous Fluid Flow*. McGraw-Hill.

YANG, Z. & VOKE, P. R. 2001 Large-eddy simulation of boundary-layer separation and transition at a change of surface curvature. *J. Fluid Mech.* **439**, 305–333.

YEE, H. C., SANDHAM, N. D. & DJOMEHRI, M. J. 1999 Low-dissipative high-order shock-capturing methods using characteristic-based filters. *J. Comput. Phys.* **150** (1), 199–238.

YUAN, W., KHALID, M., WINDTE, J., SCHOLZ, U. & RADESPIEL, R. 2007 Computational and experimental investigations of low-Reynolds-number flows past an aerofoil. *Aeronaut. J.* **111** (1115), 17–29.

ZHANG, W., HAIN, R. & KÄHLER, C. J. 2008 Scanning PIV investigation of the laminar separation bubble on a SD7003 airfoil. *Exp. Fluids* **45** (4), 725–743.